Climate and relief-induced controls on the temporal variability of denudation rates in a granitic upland

Gerald Raab,[1]* Markus Egli,[1] Kevin Norton,[2] Dennis Dahms,[3] Dagmar Brandová,[1] Marcus Christl[4] and Fabio Scarciglia[5]

[1] Department of Geography, University of Zurich, Zurich, Switzerland
[2] School of Geography, Environment and Earth Sciences, Victoria University of Wellington, Wellington, New Zealand
[3] Department of Geography, University of Northern Iowa, Cedar Falls, IA USA
[4] Department of Physics, ETH, Zurich, Zurich, Switzerland
[5] Department of Biology, Ecology and Earth Sciences (DiBEST), University of Calabria, Arcavacata di Rende (CS), Italy

*Correspondence to: Gerald Raab, Department of Geography, University of Zurich, Winterthurerstrasse 190, 8057 Zurich, Switzerland. E-mail: gerald.raab@geo.uzh.ch

ESPL

Earth Surface Processes and Landforms

ABSTRACT: How soil erosion rates evolved over the last about 100 ka and how they relate to environmental and climate variability is largely unknown. This is due to a lack of suitable archives that help to trace this evolution. We determined *in situ* cosmogenic beryllium-10 (^{10}Be) along vertical landforms (tors, boulders and scarps) on the Sila Massif to unravel their local exhumation patterns to develop a surface denudation model over millennia.

Due to the physical resistance of tors, their rate of exhumation may be used to derive surface and, thus, soil denudation rates over time. We derived soil denudation rates that varied in the range 0–0.40 mm yr^{-1}. The investigated boulders, however, appear to have experienced repositioning processes about ~20–25 ka BP and were therefore a less reliable archive. The scarps of the Sila upland showed a rapid bedrock exposure within the last 8–15 ka. Overall, the denudation rates increased steadily after 75 ka BP but remained low until about 17 ka BP. The exhumation rates indicate a denudation pulse that occurred about 17–5 ka BP. Since then the rates have continuously decreased.

We identify three key factors for these developments – climate, topography and vegetation. Between 75 and 17 ka BP, climate was colder and drier than today. The rapid changes towards warmer and humid conditions at the Pleistocene–Holocene transition apparently increased denudation rates. A denser vegetation cover with time counteracted denudation.

Topography also determined the extent of denudation rates in the upland regime. On slopes, denudation rates were generally higher than on planar surfaces. By determining the exhumation rates of tors and scarps, soil erosion rates could be determined over long timescales and be related to topography and particularly to climate. This is key for understanding geomorphic dynamics under current environmental settings and future climate change. © 2019 John Wiley & Sons, Ltd.

KEYWORDS: granite landscape; Sila Massif; tor; denudation; cosmogenic nuclides

Introduction

Landscape surfaces can be very dynamic and are often driven by environment- and climate-induced changes. Although there are numerous and detailed climate archives, few attempts have been done so far to quantify soil denudation rates over time (e.g. Bajard *et al.*, 2017), due to a deficiency in continuous *in situ* records. Catchment-wide approaches are more commonly used to infer average surface lowering and denudation rates. However, such approaches make the coupling with specific landscape sites (e.g. slopes, ridges, planes) or environmental conditions difficult, as landscapes may not evolve uniformly or linearly. To understand landscape evolution more comprehensively, new approaches and (*in situ*) archives are needed that preserve the temporal signal of surface lowering over time. A recent study (Raab *et al.*, 2018) indicated that geomorphic forms of granite landscapes (Figure 1) may preserve the

denudation signal over time. Here, we explore the potential of a variety of granite landforms such as boulders, tors or scarps in more detail.

The distinction between these three landforms may appear straightforward, but the contrary is often the case. Scarps can be associated with cliffs, steep slopes or with displaced landforms (e.g. faults, landslides) that are commonly seen as bedrock outcrops along vertical or inclined surfaces that lack more detailed definition. Boulders are generally seen as rounded rock masses detached from bedrock with a diameter greater than 256 mm (Bates and Jackson, 1987) but sizes vary greatly from 25 cm to over 33 m in diameter. Boulders have also been defined as just 'more-or-less' rounded, isolated or clustered masses of standing rock (Linton, 1955).

The most ambiguous term of all of these is the 'tor'. Most famous for describing the castellated granite landscape of Dartmoor (UK), the word is broadly used for large residual
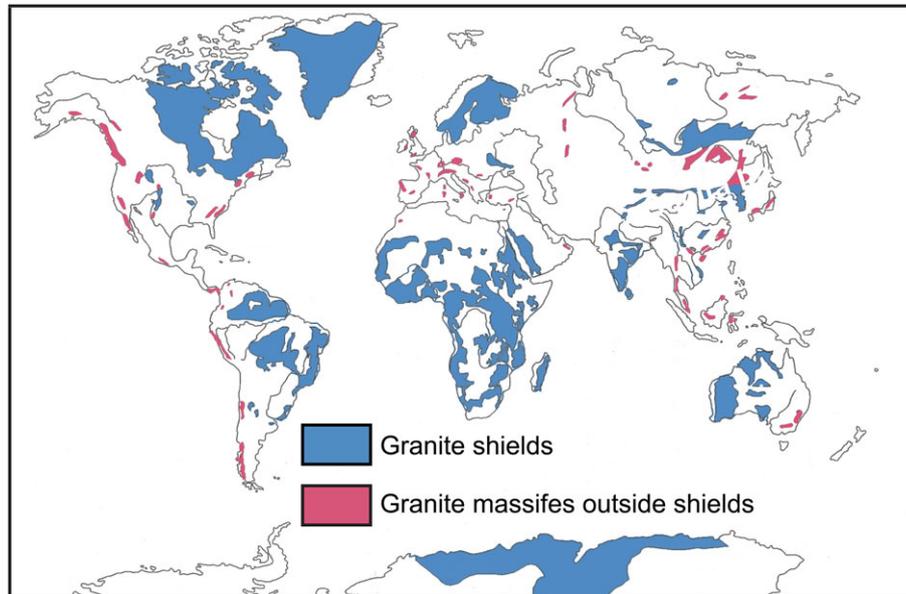
Figure 1. Granite landscapes around the world, differentiated between ancient shields and exhumed massifs. The map is modified after Migoń (2006). [Colour figure can be viewed at wileyonlinelibrary.com]

rocks (tower-like or dome-shaped), often castellated landforms (Linton, 1955). They characteristically have rounded summits or form convex ridges and seldom exceed 10–15 m in height (Migoń, 2006). Thomas (1965) described them as spherically weathered boulders which are still rooted in bedrock.

Although such granitic landscapes are ubiquitous, the geomorphic literature mostly contains conceptual models with little empirical data (Linton, 1955; Migoń, 2006; and references cited therein). The timing and the forces that enable the formation of granitic outcrops are more often qualitatively described rather than quantitatively assessed (e.g. Twidale, 2002; Phillips et al., 2006). Depending on local conditions, boulders, tors and scarps may form within the saprolite. Rock tors and boulders have higher physical resistance than the surrounding soils or saprolite that are more easily weathered (Migón and Vieira, 2014). Therefore, in an eroding landscape, tors are exhumed over time by the lowering of the surrounding surface, through surface denudation rates, $D_{Surface}$; denudation processes consisting of W, weathering [i.e. conversion of bedrock to loose (erodible) material] and E, physical erosion (transport of mobile material by e.g. wind, water):

$$D_{Surface} = W + E \qquad (1)$$

Thus, the rate of exhumation can be used to indicate denudation of the surrounding surface. Few studies have quantified the temporal development of particular landscape features (e.g. Gunnell et al., 2013, Heimsath et al., 2001). So far, granitic landforms such as tors, boulders and scarps have rarely been used as an environmental archive to trace rates of surface and relief development (Raab et al., 2018).

Vertical age profiles along tor surfaces allow the determination of their exhumation history and subsequently the calculation of surface denudation rates over several time intervals (continuous and over millennia; Heimsath et al., 2001; Wakasa et al., 2006; Raab et al., 2018). Applying the same technique to boulders and scarps enlarges the possibilities and enables comparisons among local formation patterns. Consequently, we use tors, boulders and scarps of a granitic landscape to explore surface lowering over time and, by extrapolation, past denudation rates of the surrounding landscape (predominantly erosion). Due to the fact that tors, boulders and scarps are more physically and chemically resistant than the saprolite or soil, surface

denudation causes their exhumation over time. By deriving *in situ* beryllium-10 (^{10}Be) surface exposure ages along these geomorphic landforms, we attempt to trace rates of surface lowering and, thus, soil denudation rates during the Holocene and part of the Pleistocene. We assume that denudation rates vary on both temporal and spatial scales. On eroding landscapes (and depending on the topographic position of tors, boulders or scarps), the signal intensity will most likely vary. Climate and vegetation patterns will have substantially varied over time (last 10–100 ka) in many parts of mid-latitude environments. We therefore hypothesize that calculated soil erosion rates can be linked to both the topographic position and to general patterns of climate and vegetation variability.

Study Area

The Sila Massif in Calabria (Italy) is an ideal geological and topographic setting for our study (Figure 2) with tors, boulders and rock scarps. Vegetation here consists of grassland, conifer (pine, fir) and deciduous trees (beech) (Sorriso-Valvo, 1993; Scarciglia et al., 2005a, 2005b). The present-day moist and temperate climate is typical for upland Mediterranean zones with an annual average temperature of 9 to 12°C and annual precipitation of 1000 to 1800 mm (Le Pera and Sorriso-Valvo, 2000). The landscape of the box-shaped plateau is characterized by wide-flat to gently-rolling paleosurfaces ranging between 1000 m and 1700 m above sea level (a.s.l.) that are bordered by steep slopes. The relief and drainage systems are controlled by north–south (N–S), east–west (E–W) and northwest–southeast (NW–SE) trending faults (Molin et al., 2004; Spina et al., 2007).

The geological setting (Figure 2b) of the Sila upland plateau was created by the uplift of the Paleozoic plutonic and metamorphic basement rocks of the Calabride complex and its Miocene-to-Pleistocene sedimentary cover. Regional tectonic uplift has affected a relatively large area and caused the isolation of the Sila upland through a number of tectonic phases (Molin et al., 2004; Olivetti et al., 2012). The last uplift phase occurred around 300–400 ka BP (Olivetti et al., 2012). The acceleration of regional uplift here resulted in a number of uplift rate estimates: between 0.6 and 1 mm yr^{-1} (Olivetti et al., 2012), between 0.52 and 0.88 mm yr^{-1} (Corbi et al., 2009), and 0.65 mm yr^{-1} (Bintanja et al., 2005).
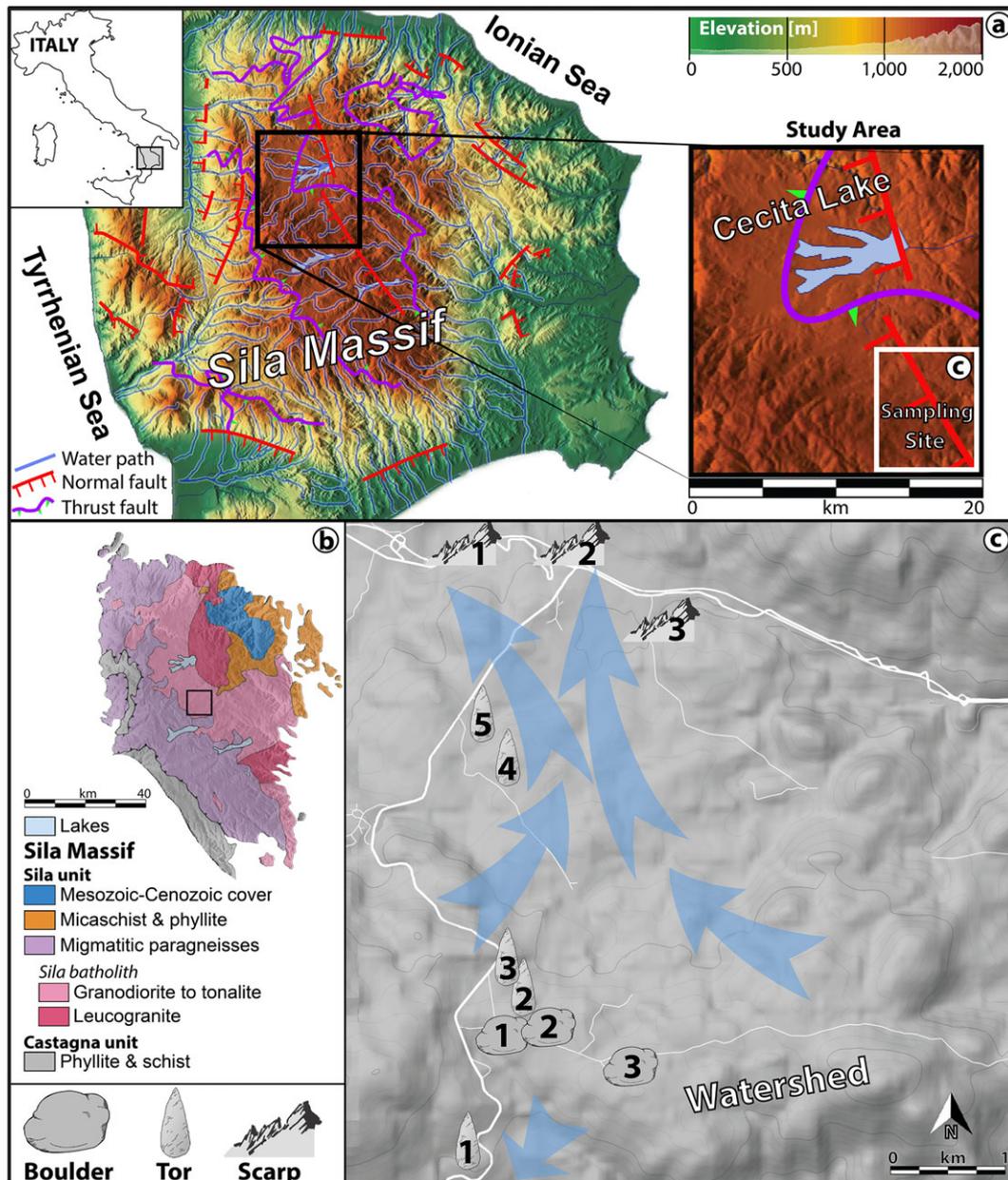
Figure 2.   (a) Topographic map of the Sila Massif in southern Italy (after Raab *et al.*, 2018). The sampling site of the study area near the Cecita Lake is marked as a white box (Geoportale Nazionale, Ministero dell'Ambiente, Italy). Additionally, normal and thrust faults are indicated (Olivetti *et al.*, 2012). (b) Geological overview map of the Sila Massif according to Liotta *et al.* (2008) and von Eynatten *et al.* (2015). The black frame indicates the sampling site. (c) Detailed position of sampled boulders, tors and bedrocks plotted on a Google map (2017) surface model together with possible drainage patterns (blue arrows) on the basis of the steepness factors from Olivetti *et al.* (2012). [Colour figure can be viewed at wileyonlinelibrary.com]

For such uplift rates, the weathering model of Thomas (1997) suggests that grus weathering slightly dominates over saprolite formation. Le Pera and Sorriso-Valvo (2000) described the local 50–60 m thick weathering mantle as 'arenite' and 'clayed grus'. Both saprolite and grus weathering mantles are identified in this region (Scarciglia *et al.*, 2016). As a consequence of local long-term deep weathering processes followed by exhumation, granitic boulder fields, tors and steep scarps have developed here which are represented by a large assortment of granitic outcrops of different sizes and shapes. Various forms depicted in the weathering scheme of Migoń (2013) are present (Raab *et al.*, 2018). Tors and outcrops with chessboard-like joint structures are found mostly along ridge crests but also occur in slightly undulating areas and isolated small topographic basins.

Tors are free-standing rock outcrops that remain attached to the underlying bedrock and usually have heights of 4 to 6 m. Some collapsed tors occur as elongated boulders with lengths of 8 m or more. Boulders, however, hardly exceed diameters

of more than 2.5 m and vary from nearly perfectly rounded to half-moon shapes. Boulders are found in clusters or as single isolates on low-angle relief surfaces. They are spread across the plateau but are more often found along gentle ridges (Scarciglia, 2015). Scarps are found throughout the plateau on rather steep to gently sloping surfaces.

Materials and Methods

Sampling sites and experimental design

Our sampling area is in the centre of the Sila massif (Figure 2a) and provides an ideal mix of all required geomorphic landforms: close proximity (Figure 2c) within a well-defined spatial area with relatively small altitudinal differences. At the centre of the sampling area is a small north-oriented basin with planation surfaces that are surrounded by gently-undulated ridges. Its

highest extent in the south acts as a divide between the northward-draining upland basin (e.g. Cecita Lake) and the southern drainage to the lowlands. Extensively-scarped slopes are mainly found in the northern basin. Tors and boulders are spread all-over, but are concentrated on the surrounding ridges.

We sampled tors from different topographic positions. Steeper slopes were investigated using one tor at the southern part of the watershed, one at the northern part and one on the ridge itself. These tors were compared to two tors nearer the basin centre with gentler slopes and to three boulders along the watershed ridge.

To determine surface denudation in this landscape, our [10]Be sampling focused on surface exposures along vertical rock profiles (Figure 3). According to our hypotheses, we expected to detect different formation and exhumation patterns:

- the vertical sampling of tors should reveal the landscape's denudation rates and changes over time and as a function of their topographic position

- boulders will have a more complex exhumation process, because of their detachment from the bedrock
- scarps probably provide the timing of relatively young denudation processes

Sampling of rocks for *in situ* [10]Be dating

We sampled five tors, three boulders and three scarps (Table I). An average of six 1–3 kg samples per tor were taken at different heights in order to assess the timing of their progressive, possibly multistep, exhumation through time. Given their uneven morphology, two of the three scarps were investigated in more detail with up to seven samples. The sampling was carried out with an electric stone saw, hammer and chisel. Because cosmic rays are distinctly attenuated within the rock, production of cosmogenic isotopes is highest directly at the surface. We therefore sampled the uppermost 1–3 cm of the rock surface
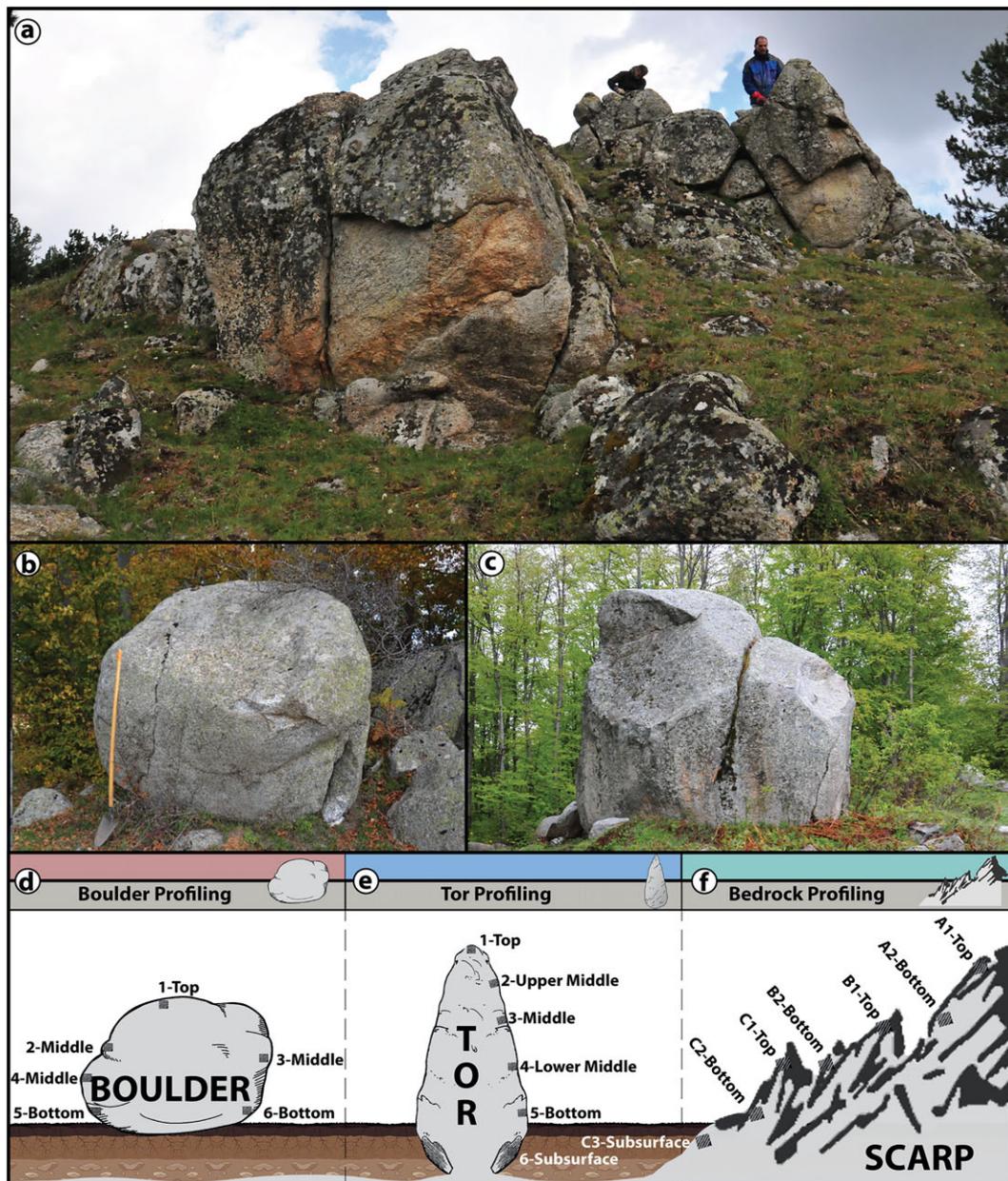
Figure 3. Overview of the sampling strategies for the individual landscape features (a,f) scarps, (b,d) boulders and (c,e) tors.. [Colour figure can be viewed at wileyonlinelibrary.com]

Table I. Sample characteristics of the investigated profiles along boulders, tors and scarps

Samples series	Coordinates [WGS84]		Ground elevation (m a.s.l.)	Rock type[b] (–)	Sample thickness (cm)	Height aboveground (m)	Dip direction of rock surface (deg)	Dip angle of rock surface (deg)	Shielding factor (–)
	Latitude (°N)	Longitude (°E)							
Boulder 1									
1-Top	39° 16′ 51.6″	16° 32′ 20.4″	1572	Granodiorite	2.00	2.25	040	10	0.999
2-Middle	39° 16′ 51.6″	16° 32′ 20.4″	1572	Granodiorite	3.00	1.28	325	70	0.613
3-Middle	39° 16′ 51.6″	16° 32′ 20.4″	1572	Granodiorite	3.00	1.02	250	80	0.879
4-Middle	39° 16′ 51.6″	16° 32′ 20.4″	1572	Granodiorite	3.00	0.76	345	85	0.558
5-Bottom	39° 16′ 51.6″	16° 32′ 20.4″	1572	Granodiorite	3.00	0.25	342	90	0.498
6-Bottom	39° 16′ 51.6″	16° 32′ 20.4″	1572	Granodiorite	3.00	0.10	220	70	0.490
Boulder 2									
1-Top	39° 16′ 51.6″	16° 32′ 20.7″	1572	Granodiorite	2.00	1.70	360	12	0.998
3-Middle	39° 16′ 51.6″	16° 32′ 20.7″	1572	Granodiorite	3.00	1.20	170	70	0.782
6-Bottom	39° 16′ 51.6″	16° 32′ 20.7″	1572	Granodiorite	9.50	−0.20	300	70	0.612
Boulder 3									
1-Top	39° 16′ 35.6″	16° 32′ 58.1″	1567	Granodiorite	1.00	1.40	047	7	1.000
6-Bottom	39° 16′ 35.6″	16° 32′ 58.1″	1567	Granodiorite	1.50	0.25	160	70	0.677
Tor 1[a]									
1-1-Top	39° 16′ 06.7″	16° 32′ 07.8″	1504	Granodiorite	2.00	4.00	150	10	0.999
1-2-Upper middle	39° 16′ 06.7″	16° 32′ 07.8″	1504	Granodiorite	3.00	2.30	270	80	0.589
1-3-Middle	39° 16′ 06.7″	16° 32′ 07.8″	1504	Granodiorite	2.50	2.10	250	80	0.544
1-4-Lower middle	39° 16′ 06.7″	16° 32′ 07.8″	1504	Granite	1.80	1.10	285	90	0.498
1-5-Bottom	39° 16′ 06.7″	16° 32′ 07.8″	1504	Granodiorite	2.00	0.20	290	40	0.473
1-6-Subsurface	39° 16′ 06.7″	16° 32′ 07.8″	1504	Granodiorite	1.00	−0.28	270	85	0.509
Tor 2[a]									
2-1-Top	39° 16′ 52.4″	16° 32′ 22.9″	1572	Granodiorite	2.00	5.60	115	32	0.972
2-2-Upper middle	39° 16′ 52.4″	16° 32′ 22.9″	1572	Granodiorite	3.00	4.60	115	80	0.654
2-3-Middle	39° 16′ 52.4″	16° 32′ 22.9″	1572	Granodiorite	1.50	3.30	225	70	0.704
2-4-Lower middle	39° 16′ 52.4″	16° 32′ 22.9″	1572	Granodiorite	2.00	2.40	245	60	0.771
2-5-Bottom	39° 16′ 52.4″	16° 32′ 22.9″	1572	Granodiorite	3.00	0.30	360	90	0.501
2-6-Subsurface	39° 16′ 52.4″	16° 32′ 22.9″	1572	Granodiorite	9.50	−0.20	300	70	0.724
Tor 3[a]									
3-1-Top	39° 17′ 01.6″	16° 32′ 17.0″	1569	Granodiorite	2.00	3.50	358	10	0.999
3-2-Upper middle	39° 17′ 01.6″	16° 32′ 17.0″	1569	Granodiorite	3.00	2.10	170	85	0.504
3-3-Middle	39° 17′ 01.6″	16° 32′ 17.0″	1569	Granodiorite	2.00	1.30	165	90	0.498
3-4-Lower middle	39° 17′ 01.6″	16° 32′ 17.0″	1569	Granodiorite	4.00	1.10	165	90	0.498
3-5-Bottom	39° 17′ 01.6″	16° 32′ 17.0″	1569	Granodiorite	2.00	0.20	170	80	0.607
3-6-Subsurface	39° 17′ 01.6″	16° 32′ 17.0″	1569	Granodiorite	3.00	−0.40	170	90	0.601
Tor 4									
4-1-Top	39° 17′ 56.9″	16° 32′ 20.6″	1465	Granite	3.00	3.60	030	44	0.926
4-2-Upper middle	39° 17′ 56.9″	16° 32′ 20.6″	1465	Granite	3.00	2.00	170	80	0.612
4-3-Middle	39° 17′ 56.9″	16° 32′ 20.6″	1465	Granodiorite	3.00	1.55	170	80	0.612
4-4-Lower middle	39° 17′ 56.9″	16° 32′ 20.6″	1465	Granodiorite	3.00	0.85	170	80	0.612
4-5-Bottom	39° 17′ 56.9″	16° 32′ 20.6″	1465	Granite	3.00	0.38	170	80	0.612
4-6-Subsurface	39° 17′ 56.9″	16° 32′ 20.6″	1465		3.00	−0.30	170	80	0.612
Tor 5									
5-1-Top	39° 18′ 02.4″	16° 32′ 12.4″	1475	Granite	2.00	2.40	088	26	0.986
5-2-Upper middle	39° 18′ 02.4″	16° 32′ 12.4″	1475	Granite	1.50	1.60	071	21	0.969
5-3-Middle	39° 18′ 02.4″	16° 32′ 12.4″	1475	Granite	3.00	1.40	081	30	0.964
5-4-Lower middle	39° 18′ 02.4″	16° 32′ 12.4″	1475	Granite	2.20	1.10	029	11	0.983
5-5-Bottom	39° 18′ 02.4″	16° 32′ 12.4″	1475	Granodiorite	1.80	0.26	160	55	0.845
5-6-Subsurface	39° 18′ 02.4″	16° 32′ 12.4″	1475	Granodiorite	1.80	−0.20	164	76	0.528
Scarp 1									
C1-Top	39° 19′ 06.1″	16° 32′ 12.8″	1360	Granite	3.00	1.49	285	10	0.932
Scarp 2									
A1-Top	39° 19′ 06.4″	16° 32′ 35.2″	1394	Granite	2.50	0.50	210	50	0.890
A2-Bottom	39° 19′ 06.4″	16° 32′ 35.2″	1394	Granite	2.50	0.10	110	80	0.534
B1-Top	39° 19′ 06.4″	16° 32′ 35.2″	1393	Granite	2.50	2.00	270	30	0.977
B2-Bottom	39° 19′ 06.4″	16° 32′ 35.2″	1393	Granite	2.50	1.00	270	90	0.492
C1-Top	39° 19′ 06.4″	16° 32′ 35.2″	1393	Granite	2.50	2.30	105	10	0.997
C2-Bottom	39° 19′ 06.4″	16° 32′ 35.2″	1393	Granite	2.50	1.10	210	70	0.714
C3-Subsurface	39° 19′ 06.4″	16° 32′ 35.2″	1393	Granite	2.50	−0.35	200	70	0.710
Scarp 3									
A1-Top	39° 18′ 43.2″	16° 33′ 22.3″	1422	Granite	1.30	0.75	228	28	0.982
A2-Bottom	39° 18′ 43.2″	16° 33′ 22.3″	1413	Granite	2.00	0.20	195	30	0.978

(*Continues*)

Table 1. (Continued)

Samples series	Coordinates [WGS84]		Ground elevation (m a.s.l.)	Rock type[b] (–)	Sample thickness (cm)	Height aboveground (m)	Dip direction of rock surface (deg)	Dip angle of rock surface (deg)	Shielding factor (–)
	Latitude (°N)	Longitude (°E)							
B1-Top	39° 18′ 43.2″	16° 33′ 22.3″	1413	Granite	1.50	0.95	233	12	0.993
B2-Bottom	39° 18′ 43.2″	16° 33′ 22.3″	1413	Granite	1.50	0.15	055	40	0.991
C1-Top	39° 18′ 43.2″	16° 33′ 22.3″	1413	Granite	1.50	0.87	240	10	0.992
C2-Bottom	39° 18′ 43.2″	16° 33′ 22.3″	1413	Granite	3.00	0.64	240	30	0.977
C3-Subsurface	39° 18′ 43.2″	16° 33′ 22.3″	1413	Granite	1.80	−0.20	210	35	0.967

[a]Data from Raab et al. (2018).
[b]Classification after Middlemost (1994).

(Table I). Since tors may have already interacted with cosmogenic rays before they appear at the ground surface, we also sampled belowground (up to 40 cm deep) to account for possible early subsurface ^{10}Be accumulation. This was necessary in order to constrain the exhumation models. The position (latitude, longitude, altitude) of the sampling sites was recorded with global positioning system (GPS) and verified with topographic maps. Standard corrections were made for the geometry of the rock samples and the effect of topographic shielding at each location (Gosse and Philips, 2001).

Surface exposure dating laboratory procedure – ^{10}Be

The rock sample material was crushed and about 0.4 kg of the 0.6–0.25 mm fraction was collected and treated according to standard procedures (Kohl and Nishiizumi, 1992). The selected fraction was treated with *aqua regia* for up to 36 hours and iron oxides, organic material and carbonates were eliminated. The remaining mineral assemblage underwent a one hour-treatment with 0.4% hydrogen fluoride (HF). Afterwards we used a flotation system (Kitchener, 1984) to physically separate mica and feldspar components from quartz. Any remaining contaminants were removed with 4% HF leaching cycles (7–21 days). About 20–30 g of the obtained pure quartz were spiked with a ^{9}Be-carrier solution (Scharlau, BE03460100) and together dissolved in 40% HF. We isolated Be by using anion and cation exchange columns followed by selective pH precipitation (von Blanckenburg et al., 1996). The resulting beryllium hydroxide (Be (OH)$_2$) was calcinated to beryllium oxide (BeO) for two hours at 850°C and mixed with niobium (Nb) powder before pressing it into copper (Cu)-targets. The ETH Laboratory of Ion Beam Physics accelerator mass spectrometry (AMS) facility measured the targets. ETH used ^{10}Be standard S2007 N with a nominal value of ^{10}Be/^{9}Be = 28.1 × 10^{-12} calibrated to the Nishiizumi standard ICN01-5-1 with a revised nominal value of 2.709 × 10^{-11} (Christl et al., 2013; Kubik and Christl, 2010; Nishiizumi et al., 2007). The 1σ error of S2007 N is 2.7% (Christl et al., 2013). The measured ^{10}Be/^{9}Be ratios were corrected for the ^{10}Be contribution of the Be-carrier (^{10}Be/^{9}Be blank ratio: 3.00 ± 0.87 × 10^{-15}). Exposure ages were calculated using the cosmogenic nuclide online calculator v2.3 (Balco et al., 2008). The programme uses a ^{10}Be half-life of 1.387 ± 0.0012 Ma (Chmeleff et al., 2010; Korschinek et al., 2010) and a sea level high latitude ^{10}Be production rate of 4.01 ^{10}Be-atoms g^{-1} SiO$_2$ yr^{-1} (Borchers et al., 2016). The production rate was corrected for latitude and altitude after the scaling scheme of Stone (2000) and further corrected for the sample thickness according to the depth profile of Brown et al. (1992) with an effective radiation attenuation length of 160 g cm^{-2} of Gosse and Philips (2001) and a constant rock density of 2.7 g cm^{-3}. A variety of rock surface erosion rates were tested with no correction for snow. Related effects of geomagnetic field variations on the ^{10}Be ages are assumed to be negligible (Masarik et al., 2001; Pigati and Lifton, 2004).

Determination of surface denudation rates ($D_{Surface}$)

Ages were calculated on the basis of a rock surface erosion rate between 0 and 0.002 mm yr^{-1}, typical for cold (alpine) granite regions (Small et al., 1999), and were subsequently used for modelling the exhumation rate (height versu age). Best regression fits were obtained with a polynomial (third order) or a logistic function (Lichter, 1998) given by

$$f(t) = \frac{a}{(1 + e^{b(t-c)})} + d \qquad (2)$$

where *f*(*t*) is the height in metres (lowered surface), as a function of time, *a* is the range of height in metres, *t* time in years, *b* the slope coefficient, *c* the time of the maximal rate of change in years, and d the asymptotic value in metres. The height–age relation of the exhuming tors was then modelled by taking the error ranges of the ^{10}Be measurements into account (external error), using Monte Carlo simulations and the previously noted regression fits.

The mathematical derivative of these functions then provided the rates of surface lowering and, thus, surface denudation ($D_{Surface}$) in millimetres per year. For this calculation, it was necessary to account for the age of the rocks' initial surface appearance (early subsurface ^{10}Be accumulation; t_s), as follows:

$$D_{Surface} = \frac{\partial f_{(t-t_s)}}{\partial t} \qquad (3)$$

Results

Tors

The 30 samples collected from tors (Table I) resulted in 24 ages ranging from 11 ± 2 ka to 106 ± 12 ka (Table II, Table S1). Application of various surface erosion rates (0, 0.001, 0.002 mm yr^{-1}) resulted only in minor differences (about 2.6 ka) in the exposure ages. Use of a surface erosion rate of 0.002 mm yr^{-1} resulted in the following age–height relationships: 38 ± 4 ka at 4 m for tor #1, 106 ± 12 ka at 5.6 m for tor #2, 37 ± 4 at 3.5 m for tor #3, 32 ± 3 ka at 3.6 m for tor #4 and 33 ± 3 at 2.4 m for tor #5 (Figure 4).

The series of vertical profile samples from the five tors showed a general increase in ^{10}Be concentration with increasing height above the surrounding ground surfaces (Figure 4f). We observed no obvious morphologic features that would indicate the presence of abrupt changes to the ^{10}Be signal (e.g. exfoliation).

© 2019 John Wiley & Sons, Ltd.

Earth Surf. Process. Landforms, Vol. **44**, 2570–2586 (2019)

Table II. Calculated exposure ages (± external uncertainty) based on ^{10}Be concentration (± error) and different rock surface erosion rates ($E0 = 0.000$ mm yr^{-1}, $E1 = 0.001$ mm yr^{-1}, $E2 = 0.002$ mm yr^{-1})

|	^{10}Be		Heights	Calculated exposure ages of different rock surface erosion rates		
	Concentration (E+4 atoms g^{-1})	Error (%)	(m)	$E0$ (a)	$E1$ (a)	$E2$ (a)
Boulder 1						
1-Top	30.24 ± 1.64	5.4	2.25	23000 ± 2341	23448 ± 2434	23919 ± 2535
2-Middle	31.47 ± 1.27	4.0	1.28	39258 ± 3742	40582 ± 4003	42032 ± 4303
3-Middle	69.83 ± 2.80	4.0	1.02	61382 ± 5880	64733 ± 6553	68625 ± 7399
4-Middle	34.40 ± 3.41	9.9	0.76	47197 ± 6243	49129 ± 6775	51287 ± 7405
5-Bottom	28.40 ± 2.11	7.4	0.25	43504 ± 4977	45134 ± 5364	46937 ± 5817
6-Bottom	50.10 ± 2.97	5.9	0.10	78674 ± 8339	84265 ± 9603	91069 ± 11315
Boulder 2						
1-Top	26.52 ± 1.36	5.1	1.70	21643 ± 2168	22038 ± 2249	22454 ± 2336
6-Bottom	16.73 ± 0.85	5.1	−0.20	23519 ± 2348	23984 ± 2443	24475 ± 2546
Boulder 3						
1-Top	64.35 ± 1.77	2.8	1.40	49367 ± 4483	51502 ± 4886	53903 ± 5367
6-Bottom	7.03 ± 0.35	5.0	0.25	7828 ± 776	7878 ± 786	7930 ± 797
Tor 1[a]						
1-1-Top	44.99 ± 2.51	5.6	4.00	36094 ± 3716	37215 ± 3954	38434 ± 4224
1-2-Upper middle	19.95 ± 0.78	3.9	2.30	27097 ± 2561	27717 ± 2682	28376 ± 2814
1-3-Middle	18.42 ± 0.71	3.8	2.10	26987 ± 2542	27602 ± 2661	28255 ± 2791
1-4-Lower middle	16.60 ± 0.67	4.0	1.10	26327 ± 2502	26910 ± 2616	27529 ± 2740
1-5-Bottom	11.08 ± 0.49	4.5	0.20	18479 ± 1788	18763 ± 1844	19059 ± 1904
1-6-Subsurface	12.18 ± 0.57	4.6	−0.28	18748 ± 1831	— ± —	— ± —
Tor 2[a]						
2-1-Top	112.44 ± 4.39	3.9	5.60	89330 ± 8576	96723 ± 10097	106044 ± 12269
2-2-Upper middle	70.94 ± 2.70	3.8	4.60	83960 ± 8016	90408 ± 9332	98390 ± 11161
2-4-Lower middle	30.12 ± 1.49	4.9	2.40	29647 ± 2946	30395 ± 3098	31195 ± 3267
2-5-Bottom	6.96 ± 1.40	20.0	0.30	10518 ± 2297	10609 ± 2338	10703 ± 2380
2-6-Subsurface	13.82 ± 0.72	5.2	−0.20	15328 ± 1538	— ± —	— ± —
Tor 3[a]						
3-1-Top	45.45 ± 1.04	2.3	3.50	34745 ± 3097	35782 ± 3287	36906 ± 3501
3-3-Middle	18.18 ± 0.56	3.1	1.30	27578 ± 2518	28219 ± 2638	28901 ± 2770-
3-4-Lower middle	19.73 ± 0.57	2.8	1.10	28872 ± 2616	29576 ± 2747	30328 ± 2892
3-5-Bottom	16.76 ± 0.57	3.4	0.20	20882 ± 1927	21248 ± 1996	21931 ± 2069
Tor 4						
4-1-Top	34.14 ± 0.84	2.5	3.60	30556 ± 2736	31353 ± 2882	32207 ± 3045
4-2-Upper middle	23.82 ± 0.70	2.9	2.00	32088 ± 2918	32963 ± 3082	33906 ± 3265
4-4-Lower middle	13.24 ± 0.46	3.4	0.85	17775 ± 1646	18038 ± 1696	18313 ± 1749
4-5-Bottom	8.58 ± 0.30	3.5	0.38	11493 ± 1062	11603 ± 1083	11715 ± 1104
Tor 5						
5-1-Top	37.73 ± 1.31	3.5	2.40	31258 ± 2903	32093 ± 3062	32990 ± 3240
5-2-Upper middle	31.23 ± 1.50	4.8	1.60	26164 ± 2578	26745 ± 2695	27362 ± 2823
5-4-Lower middle	33.04 ± 1.11	3.4	1.10	27477 ± 2538	28119 ± 2659	28803 ± 2793
5-5-Bottom	22.54 ± 0.84	3.7	0.26	21661 ± 2028	22057 ± 2103	22472 ± 2184
5-6-Subsurface	20.86 ± 1.20	5.7	−0.20	31963 ± 3314	32830 ± 3499	33763 ± 3706
Scarp 1						
C1-Top	15.05 ± 0.81	5.4	1.49	14391 ± 1459	14564 ± 1494	14742 ± 1532
Scarp 2						
A1-Top	11.16 ± 0.67	6.0	0.50	10847 ± 1134	10944 ± 1154	11045 ± 1176
B1-Top	13.30 ± 0.54	4.0	2.00	11793 ± 1117	11908 ± 1139	12027 ± 1163
B2-Bottom	7.36 ± 0.39	5.3	1.00	12831 ± 1296	12967 ± 1323	13107 ± 1353
C1-Top	12.00 ± 0.43	3.3	2.30	11294 ± 1037	11400 ± 1057	11509 ± 1077
C2-Bottom	9.51 ± 0.39	4.1	1.10	11494 ± 1091	11603 ± 1112	11716 ± 1134
C3-Subsurface	7.01 ± 0.35	4.9	−0.35	8501 ± 840	8561 ± 852	8622 ± 864
Scarp 3						
A1-Top	9.82 ± 0.46	4.7	0.75	8393 ± 819	8345 ± 830	8511 ± 842
B1-Top	14.04 ± 0.88	6.2	0.95	11896 ± 1262	12014 ± 1287	12136 ± 1313
C1-Top	9.78 ± 0.52	5.4	0.87	8288 ± 837	8345 ± 848	8403 ± 860
C2-Bottom	10.35 ± 0.80	7.7	0.64	9014 ± 1039	9081 ± 1055	9150 ± 1071

Note: Calculation was performed using the cosmogenic nuclide online calculator v2.3 (Balco *et al.*, 2008).
[a]Data from Raab *et al.* (2018).

Samples taken below the present-day surface to determine early subsurface ^{10}Be accumulation had similar atom counts to those samples taken from the land-surface level at the base of the tors.

Following Raab *et al.* (2018), we used the surface ages, and thus exhumation rates, of the individual tors to model the surface denudation rates (Figures 5b, 5d, 5f, 6b and 6d). We calculated average exhumation rates ($\approx D_{\text{Surface}}$) of 0.062 ± 0.037 mm yr^{-1}, 0.044 ± 0.023 mm yr^{-1}, 0.046 ± 0.036 mm yr^{-1}, 0.062 ± 0.035 mm yr^{-1} and 0.036 ± 0.031 mm yr^{-1} for Tors #1–#5, respectively (rock surface erosion rate of 0.002 mm yr^{-1}). From the greater heights and older ages of the samples from Tor #2, we were able to model soil denudation rates for the last ~100 ka. Tor #2 yielded unusually low soil denudation rates compared to the other tors. Between 20 and 25 ka BP
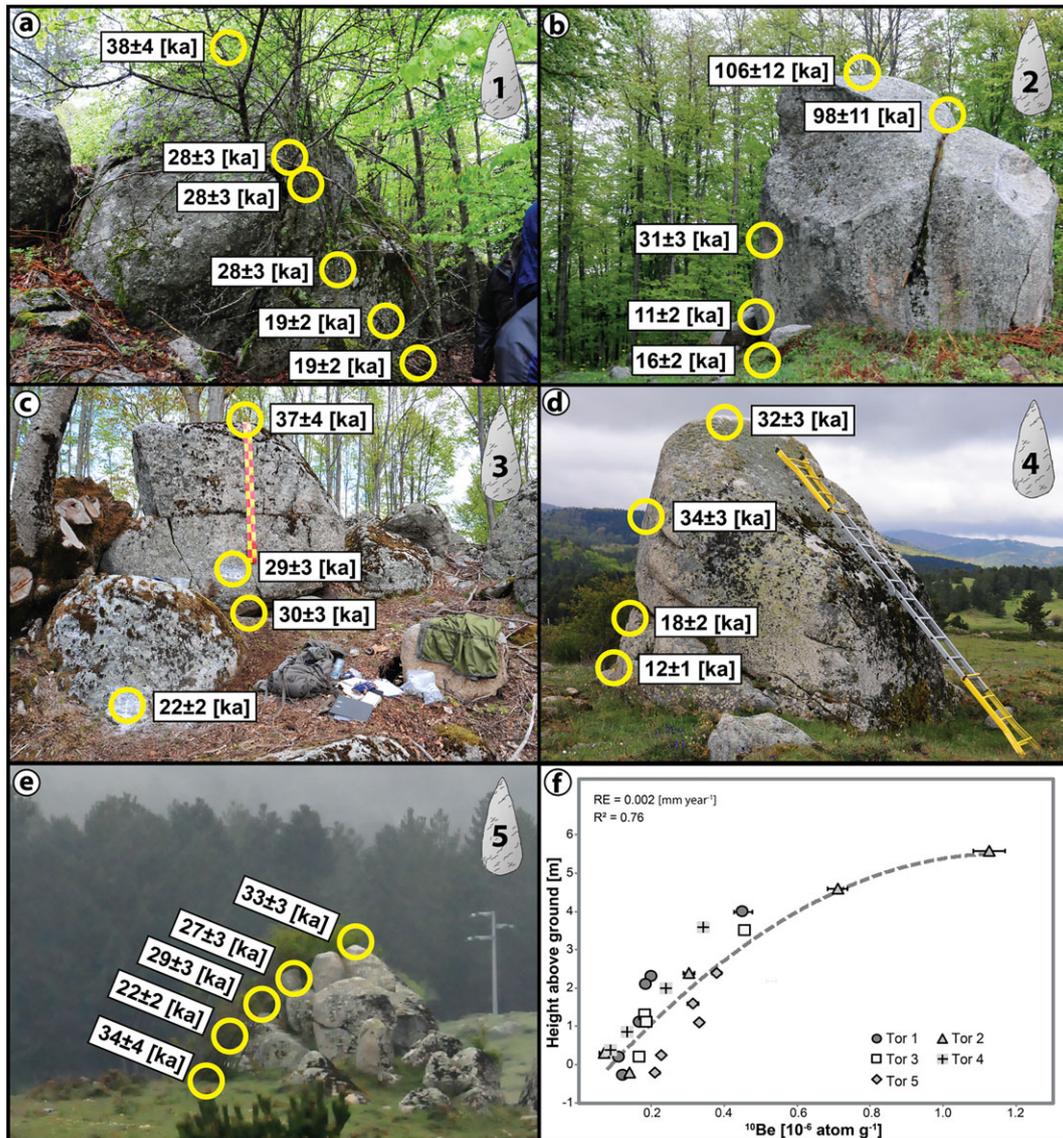
Figure 4. Exposure ages (a–e) along the tor profiles (Table II; $E2 = 0.002$ mm yr^{-1}). The overall ^{10}Be concentrations as a function of height (with related trend curve) of all samples are plotted in (f). [Colour figure can be viewed at wileyonlinelibrary.com]

(Figure 5d), however, Tor #2 exhibits similar results to the others. Tors #1 and #3 have similar slope angles (~6°–10°) and similar surface ages at similar heights. Both exhibit similar denudation rates (Figures 5b and 5f) in the range 0.05–0.37 mm yr^{-1}. The surface denudation rates derived from the exhumation rates of tors having slope angles of 0° to 2° (Tors #4 and #5) are slightly lower (0.06–0.22 mm yr^{-1}; Figures 6b and 6d).

Boulders

The 11 boulder samples (Table I) provided 10 surface exposure ages (Table II) that vary from 8 ± 1 ka to 91 ± 11 ka (Figure 7). The range of ages obtained from the boulders is similar to that of the tors, but all ages and ^{10}Be concentrations show broad variation at the same heights aboveground. The oldest age was from the sample taken at the bottom of Boulder #1, while the youngest ages were from the top of Boulder #2 and the bottom of Boulder #3. Using a surface erosion rate of 0.002 mm yr^{-1}, the top sample (1.4 m) of Boulder #3 resulted in an age of 54 ± 5 ka, similar to the ages (42 ± 4 to 68 ± 7 ka) of samples taken at the half total height (0.76–1.28 m) at Boulder #1. Boulder #2 gives nearly identical ages at the top (22 ± 2 ka) and at the bottom (24 ± 3 ka) despite a height difference of 1.7 m.

Scarps

The 15 samples taken along scarps (Table I) resulted in 11 measured ages ranging from 8 ± 1 ka to 15 ± 2 ka (Table II; Figure 8). Scarp #1 yielded the oldest age, but only one sampled was measured here. Scarps #2 and #3 exhibit identical ages at their base (9 ± 1 ka). The ages slightly increase with height up to 13 ± 1 ka at Scarp #2. At Scarp #3, however, the top of the scarp still exhibited an age of 9 ± 1 ka while the ages at the bottom are similar to Boulder #3 (8 ± 1 ka). The larger number of successfully dated samples from Scarp #2 (six samples) enabled us to derive an age–height model and subsequently a soil denudation trend model, which integrated the results from the individual samples of Scarp #1 (one sample) and Scarp #3 (four samples). The denudation rates range from 0.06 to 0.40 mm yr^{-1} with a peak denudation rate at *c.* 4 ka BP (Figures 6e and 6f).

Discussion

Tors

We see the increases in ^{10}Be concentrations with height (Figure 4f) as validation of our conceptual idea that tors were

© 2019 John Wiley & Sons, Ltd.

Earth Surf. Process. Landforms, Vol. **44**, 2570–2586 (2019)
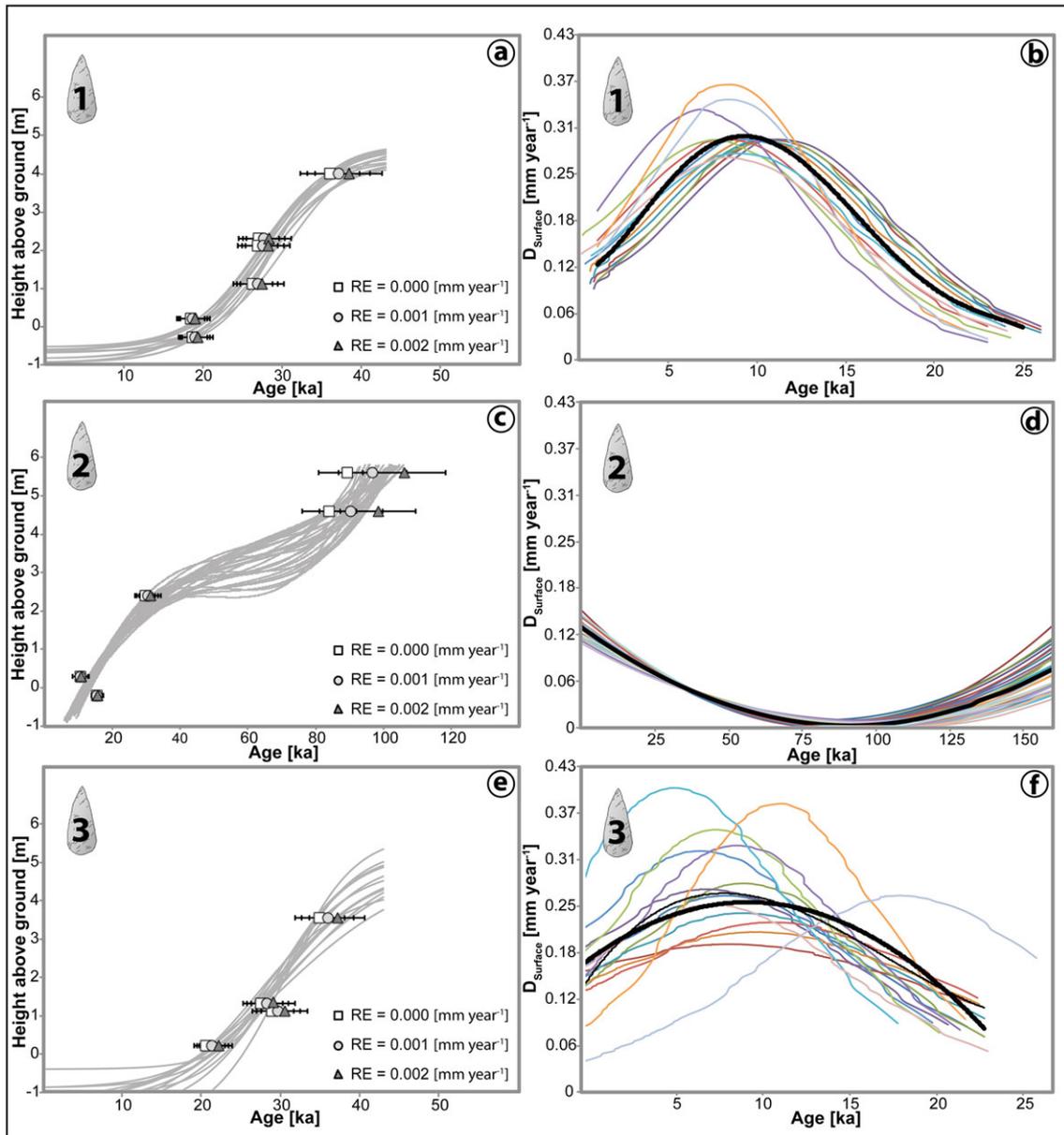
Figure 5. Trend of exposure ages as a function of tor height and derived soil denudation rates ($D_{Surface}$) using Monte Carlo simulations for Tor #1 (a and b), Tor #2 (c and d) and Tor #3 (e and f). RE = rock erosion. [Colour figure can be viewed at wileyonlinelibrary.com]

exhumed gradually over time (Figure 9). A search of the literature shows that surface denudation rates using granite tors are about 0.01–0.02 mm yr^{-1} for cold (alpine) regions (Small *et al.*, 1999) and 0.01–0.09 mm yr^{-1} in cool temperate climates (Heimsath *et al.*, 2001; Phillips *et al.*, 2006; Gunnell *et al.*, 2013). Our average exhumation rates (0.03–0.10 mm yr^{-1}) fit well to those reported from the Dartmoor tors (Gunnell *et al.*, 2013). Using river sediments as tracers, Olivetti *et al.* (2012) reported similar average erosion rates from cosmogenic ^{10}Be concentrations for the low-relief surfaces of the Sila upland (0.09 ± 0.01 to 0.13 ± 0.01 mm yr^{-1}). Our approach, however, allows us to not only report an average value, but also to capture the variations over a time span of about 100 ka.

The exhumation rates of tors depend on their topographic position. Tors found at similar topographic positions exhibit similar denudation trends. Tors #1 and #3 are positioned along backslopes and show higher overall rates (Figures 5b and 5d) than Tors #4 and #5 (Figures 6b and 6d), which are near the basin floor and along a lower surface gradient. These results show that tor archives can be used to decrypt differences in intensity and timing of denudation as well as variations among different

slope segments over millennia. The regional character of the Sila uplift (Molin *et al.*, 2004; Olivetti *et al.*, 2012) corresponds with these general exhumation trends.

Boulders

The complex age–elevation relationships imply that the boulders probably are not in their original position which supports our hypothesis that some boulders have moved. Because of these inconsistencies, we were unable to derive exhumation rates from these boulders. Re-location due to a collapse of a larger structure, rock spallation, exfoliation (Scarciglia *et al.*, 2005a, 2007) and toppling are plausible reasons for the various exposure ages. The selective local spheroidal weathering process is still continuing today (Scarciglia, 2015). A chemical weathering-driven multi-stage development of boulder landforms was proposed by Twidale (2002) through the formation of 'corestones' prior to exhumation (Migoń and Prokop, 2013). This process is most notable in grus weathering environments, where the corestones emerge as boulders (Twidale and
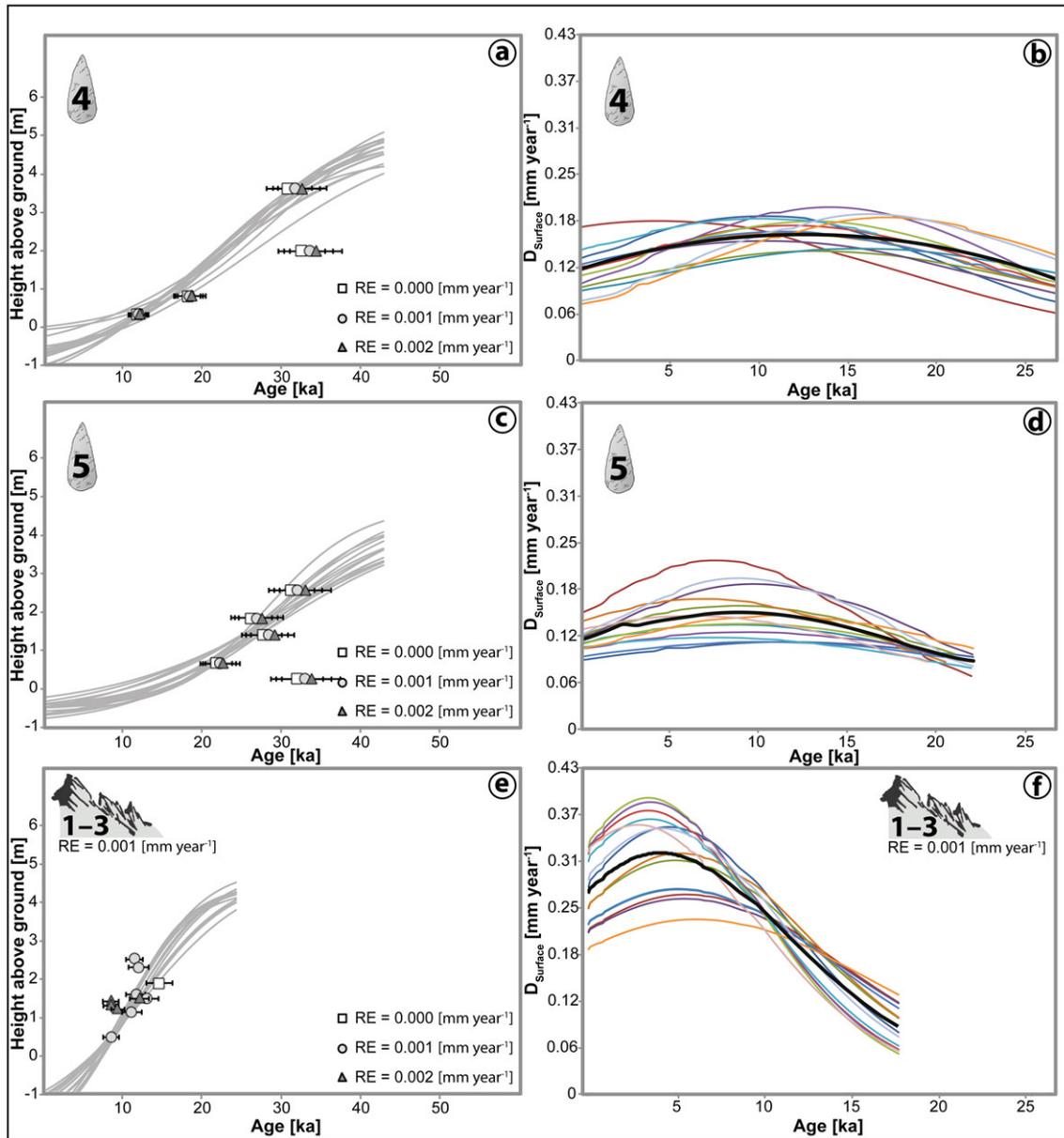
Figure 6. Exposure ages as a function of sample height/tors and scarps) and derived surface denudation rates ($D_{Surface}$) using Monte Carlo simulations for Tor #4 (a and b), Tor #5 (c and d) and Scarps #1–#3 (e and f). RE = rock erosion. [Colour figure can be viewed at wileyonlinelibrary.com]

Romaní, 2005). The fast removal of material surrounding the corestones, via e.g. physical erosion, could also be a relevant factor that leads to the emergence of boulders, as it reduces the time needed for a continuous chemical weathering.

Depending on the boulders' positions within the rock mass and the intensity of the erosion process, a broad spectrum of exhumation events is likely, from gradual (Boulder #3) to abrupt (Boulder #2).

Early exposure of some boulder margins must have occurred ~90–100 ka ago. During this phase, the tor-based denudation rates were low (Figure 5d). Through constant denudation, progressively lower portions of boulders were exposed to cosmic rays. Thus, a second phase of exposure seems to have occurred ~50–70 ka ago (Figure 7; Table II) and coincides with the start of the increase in surface denudation found with tors (Figure 5d). The toppling or collapse of a larger structure may have caused a repositioning of the boulders ~20–25 ka ago (Figure 10), resulting in the younger ages found at the present-day boulder tops. A final denudation pulse, indicated by the extrapolated rates from the tors on the slopes on both sides of the watershed (Figures 5b and 5f), exposed even lower parts of some boulders

(e.g. Boulder #3) around 8 ± 1 ka. Because the boulder dataset is not conclusive, we propose that both processes, single corestone exhumation and toppling may be present.

Scarps

Based on the exhumation patterns of the scarps, the soil denudation rates range from 0.06 to 0.40 mm yr^{-1} and differ from the tor-based rates in two ways: (1) their maximum denudation rates are slightly higher than those of the tors (Figures 5b, 5f, 6b and 6d) and (2) the maximum soil denudation pulse seems to have occurred at about ~4 ka BP (Figure 6f). Note that the denudation peak seen for the tors of the slopes and the planes is around ~9–14 ka BP (Figures 5b, 5f, 6b and 6d). Denudation seems to have decreased along the slopes between ~4–9 ka BP while it increased at the scarp sites (Figures 5 and 6). The exposure ages found lower on the scarps indicate that they represent the final stage of surface evolution (Figure 11) and mark the final exhumation step of some tors (Figure 4d) and one boulder (Figure 7c). We see this as a confirmation of our initial
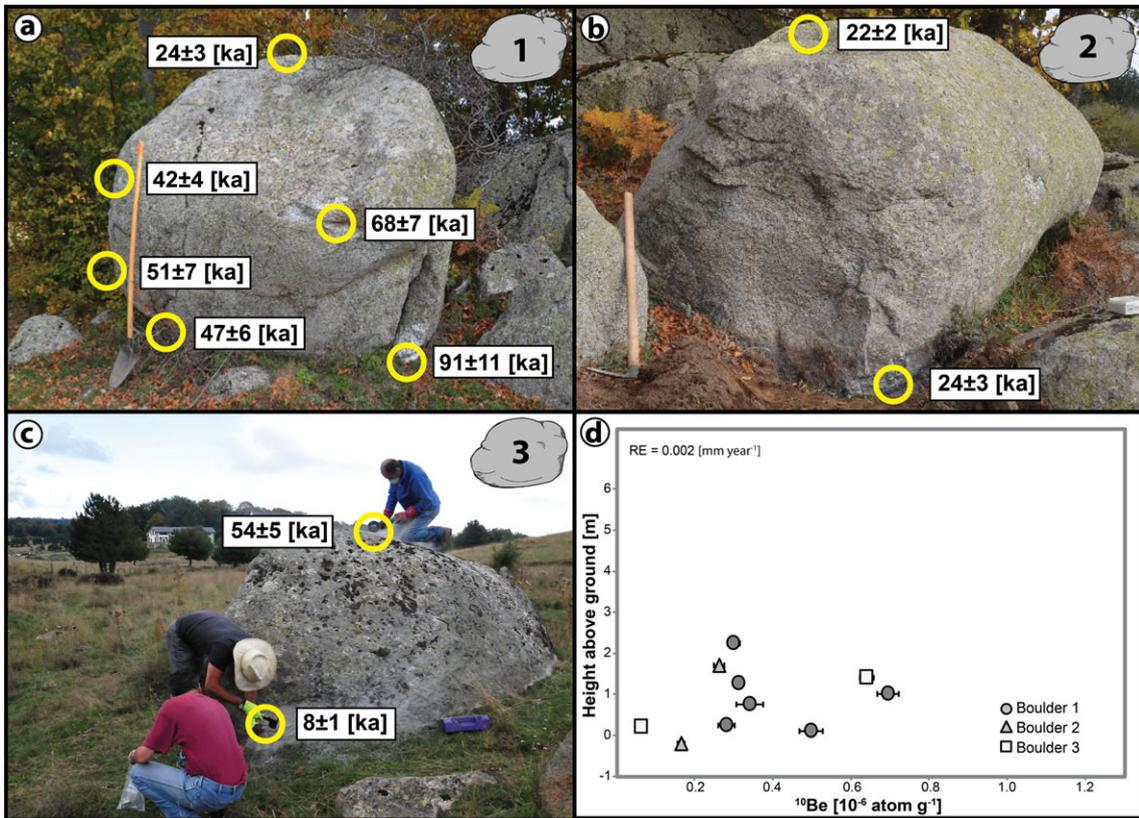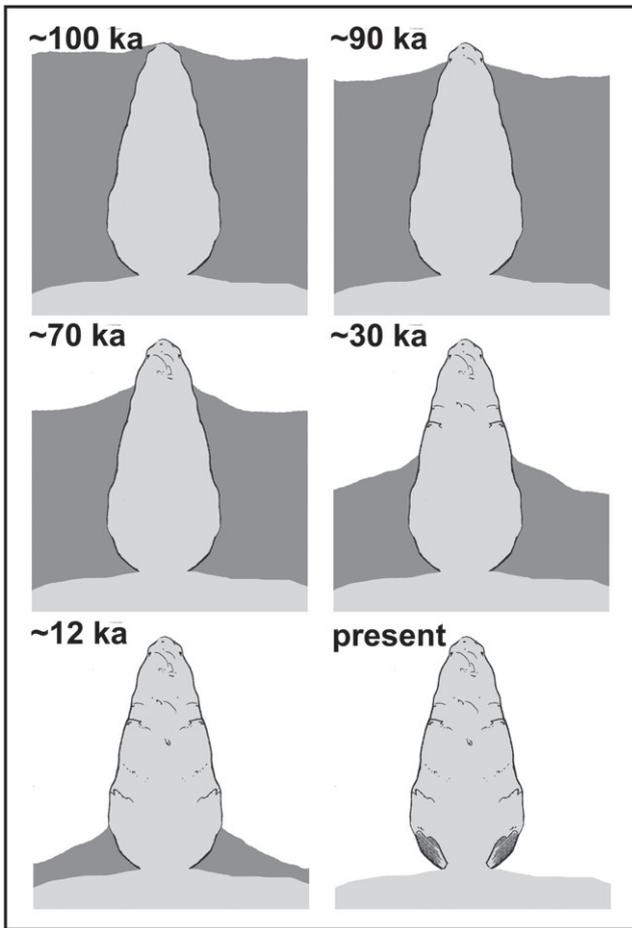
Figure 7. Exposure ages (a–c) along the boulder profiles (Table II; *E*2 = 0.002 mm yr^{-1}). Their [10]Be concentrations are plotted as a function of height (d). [Colour figure can be viewed at wileyonlinelibrary.com]
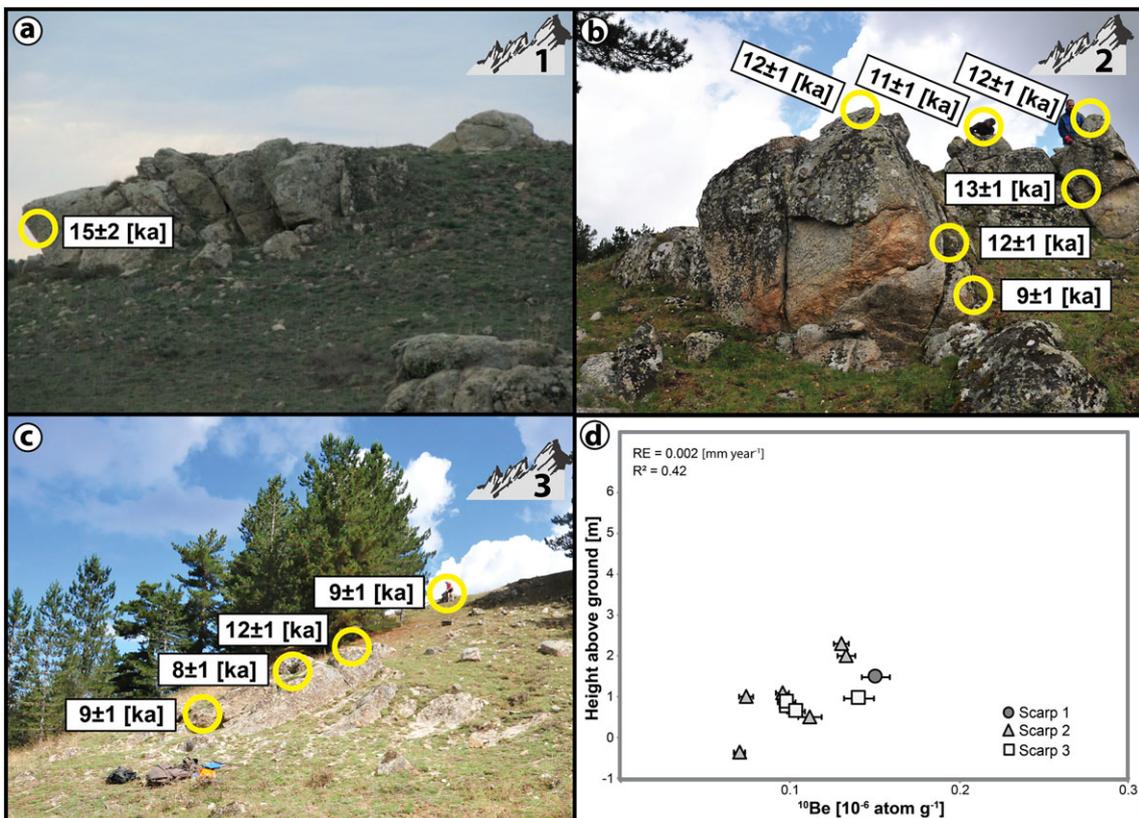
Figure 8. Exposure ages (a–c) of scarps (Table II; *E*1 = 0.002 mm yr^{-1}). Their [10]Be concentrations are plotted as a function of height (with related trend curve) in (d). [Colour figure can be viewed at wileyonlinelibrary.com]

hypothesis, that scarps represent the youngest phase in surface evolution and differ in the timing of their formation when compared to the surrounding tors and boulders. This may be related

to an episode of latest-stage headward fluvial incision toward the surrounding summits, a process which Molin *et al.* (2004) and Olivetti *et al.* (2012) have not considered. This
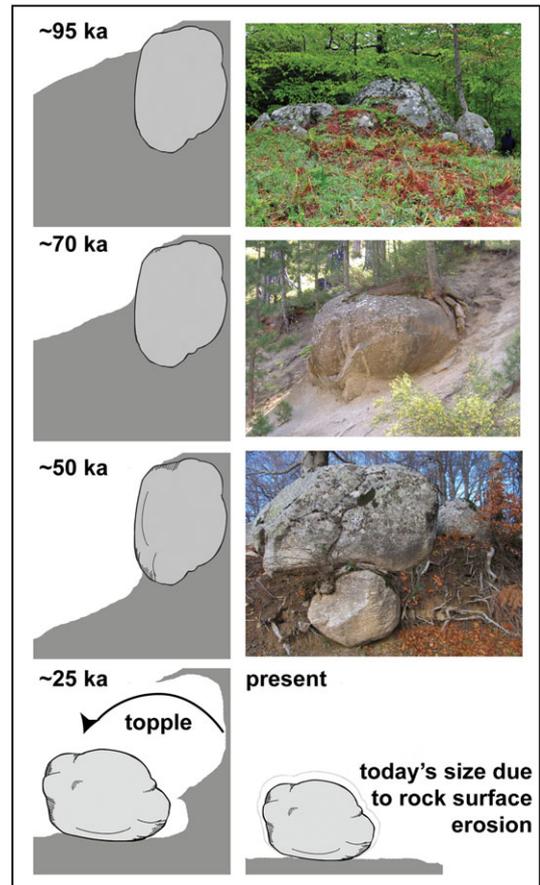
Figure 9. Concept of tor exhumation according to the surface exposure ages (e.g. Tor #2).

Figure 10. Proposed timing of events for some boulders (e.g. Boulder #1). [Colour figure can be viewed at wileyonlinelibrary.com]

interpretation also fits the concept that plateau evolution is partly a hillslope process (e.g. back-stripping; Molin *et al.*, 2004; Olivetti *et al.*, 2012).

Topography and denudation rates

So far, we establish that tors provide characteristic denudation rates within a landscape that depends on their topographic position. Boulders are not suitable for such an approach because of their detachment from the bedrock and the associated complex multi-stage exposure timing. Scarps provide only denudation trends for the most recent surface processes with similar characteristics as tors along slopes. We compare the individual modelled average denudation rates with their topographic position (Figure 12). To do this, we subdivided the relief of the study site into five distinct sections, based on their surface angle and position within the plateau (Figure 12a).

The 'ridgetops' of the watershed (Tor #2) mark the highest elevation with a minimum age of 100 ka. Exposure ages of nearby boulders indicate that some have started to form simultaneously (Figure 2c). It appears that weathered material was transferred from the ridgetops to the 'slopes' on both the northeast (Tor #3) and the southwest (Tor #1) of the ridge. These two slope sections formed no later than 60 ka after the ridgetop. The drainage and thus material transport along the southern slope (Tor #1) are directed towards the lowland (Figure 2) while the material of the northern slope (Tor #2) moves toward the small upland planes and basins where it can be partially redeposited. The Tors #4 and #5 are positioned in close proximity to a small local depression. Although these tors have only a

minimum age difference of 5 ka to those on the slopes, their denudation trends are less pronounced (Figure 12b). We interpret the lower trends as a result of exhumation buffering through sediment re-deposition. Material influx has possibly counteracted denudation at Tors #4 and #5 to slow the pace of their exhumation (Figures 6b and 6d). In summary, we see that $D_{Surface}$ started to increase at 50–75 ka BP on the ridges (Figure 5d), corresponding to the proposed second (70 ka BP) and third (50 ka BP) phases of boulder exposure (Figure 10). A subsequent phase of denudation is indicated at about 10–25 ka from the [10]Be ages of the tors. This correlates with the initiation of the toppling (e.g. collapse of larger structure) period apparent from some of the boulders (Figure 10).

Both tors and boulders are absent at the scarp sites and all are significantly older than the scarps. We propose that, during the major $D_{Surface}$ pulse (~5–15 ka BP), the slopes were strongly eroded and that the modern surfaces started to be exposed to cosmic rays at about 12 ± 1 ka (Figure 8). As the denudation rates of the surrounding area began to decrease at about 9 ± 1 ka (Figure 12b), the production of loose material also must have decreased. Due to this reduction in sediment production, it is reasonable to assume that the fluvial system of the inner plateau removed the remaining regolith rather quickly, which resulted in a rapid exposure of the scarps. The resulting sediment would then have been relocated to the surrounding flanks and in the basins at the foot of the massif (Perri *et al.*, 2012; Ruello *et al.*, 2017; Russo Ermolli *et al.*, 2018. The rapid removal of already disintegrated sediments would also explain the delayed increase in $D_{Surface}$ at the hills between 8 and 4 ka BP (Figure 12b). Because of the significant decrease in $D_{Surface}$ at the ridgetops beginning at ~9 ± 1 ka (Figures 6e, 6f and 8), the youngest tor and boulder ages (bottom of Tor #2;
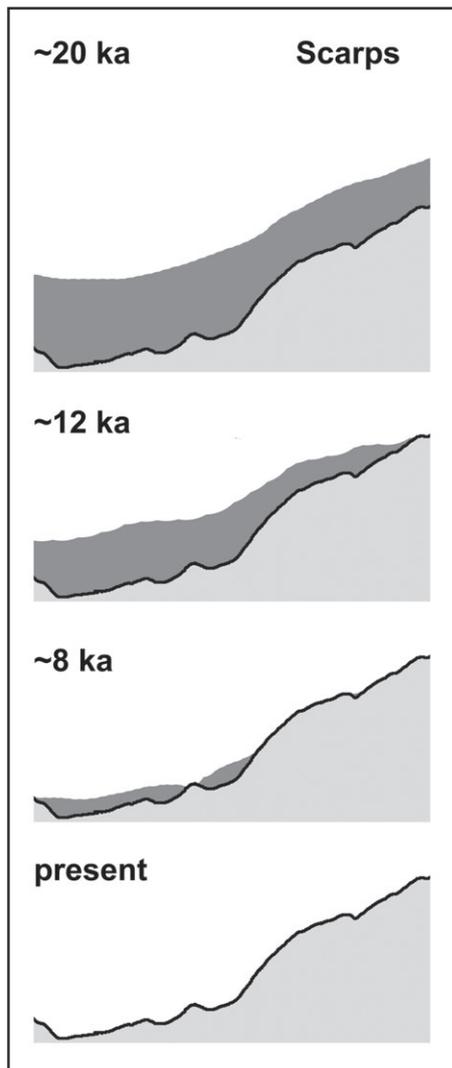
Figure 11. Conceptual model of surface lowering and exposure of scarps along the inner hills of the upland plateau.

Boulder #3; Figure 12a) match closely to those of the scarps of the hills. This suggests that the latest stage of the evolution of the Sila upland plateau was controlled by an initial episode of surface lowering followed by an early stage of river incision which then initiated erosion toward the summit of the landscape.

Responsible triggers for local denudation variations

Using the tors as an *in situ* archive, the temporal variations of the denudation rates are clearly detectable (Figures 5 and 6). Several factors determine rates of denudation, including surface topography, geology, tectonics, biosphere, human activity and climate (Smithson *et al.*, 2013). The temporal variability of the denudation rates thus suggests that the environmental drivers of landscape erosion also have changed. Furthermore, the detected changes depend on the topography, which indicates that the temporal trends depend on the relief position. Our approach and models enable us to investigate the causes of these variations over the last 100 ka (Figures 5, 6 and 12).

Because of the homogenous granitic basement (Figure 2b), abrupt lithological changes do not occur here. Therefore, other than weathering-induced changes in rock density due to saprolite formation and local tectonic effects (shear zones, fault gauges), no transition exists to move easily eroded rock types

that would have contributed to an increased $D_{Surface}$. Tectonic forces lifted the upland to its present elevation and caused a disequilibrium that had to be counterbalanced by denudation. Over the course of the investigated time span (~100 ka), the Sila Massif was uplifted by at least 50 m and possibly as much as 100 m (Bintanja *et al.*, 2005; Corbi *et al.*, 2009; Olivetti *et al.*, 2012). Our maximum denudation rate of 0.40 mm yr^{-1} (Figure 6f) would only result in a calculated absolute denudation of 40 m (in line with estimates of Scarciglia, 2015), but only if it had been constant over the entire time span. By comparing the uplift rates to the average exhumation trend (0.05 ± 0.03 mm yr^{-1}) of the vertical tor profiles, uplift appears even more dominant. Because the maximum $D_{Surface}$ is not large enough to compensate the minimum uplift-rate, we argue that the Sila Massif upland is still in disequilibrium, relative to its uplifting forces. Olivetti *et al.* (2012) also found the massif to be in a transient state of disequilibrium due to the strong and unsteady uplift that occurred 300–400 ka BP. Furthermore, our interpretation of erosion and accumulation agrees with Olivetti *et al.* (2012) who assumed that counterbalancing erosion processes (up to ~0.92 mm yr^{-1} along the massif flanks; average of ~0.13 mm yr^{-1} at plateau) are only effective along the massif flanks and that 'pre-uplift' erosion rates are conserved in the flat upland area.

Tectonic uplift processes here laid the ground work for a potential increase in $D_{Surface}$ through accentuation of the relief leading to a predisposition toward erosion. Apparently, only the surrounding flanks appear to have responded (Olivetti *et al.*, 2012) as the low $D_{Surface}$ values of the upland sites (Figures 5, 6 and 12) indicate that this area has not yet reacted to the tectonic uplift. We assume that the upland will remain relatively unaffected by the past uplift until the incision of creeks along the flanks become a dominant geomorphic process. The relatively young ages of the scarps suggest that this river incision is now at its earliest stage.

Furthermore, relief, climate and vegetation also affect soil erosion. Vegetation ('biology') is, however, not a fully independent factor because it depends on climate. Therefore, a climate effect on erosion always also includes, to a certain extent, vegetation (in the case that there is no anthropogenic impact). The uplift of the plateau also contributed to an environmental change in flora and fauna. The plateau began as a Miocene lowland 5 Ma ago, then evolved to a low-relief landscape ~2.6 Ma and finally to an upland at about 400 ka ago (Olivetti *et al.*, 2012). Based on pollen data, Fauquette and Combourieu-Nebout (2013) demonstrated that the Sila Massif had already reached a height of 1600 to 2100 m a.s.l. by 2.4 Ma. Furthermore, they described a change from a subtropical forest to an open-herbaceous biome as the uplift shifted the former humid climate towards a climate more dominated by stronger seasonal contrasts in temperature and precipitation. This change from a Thermomediterranean to an Oromediterranean and Altimediterranean altitudinal organization (Ozenda 1975; Bonin, 1981) has been identified in southern Calabria (Combourieu-Nebout, 1993).

In general, denudation forces are weaker under forest biomes and stronger in steppes, where the vegetation cover is temporally discontinuous (Allen *et al.*, 1999). Forest biomes dominated the mountain regions of southern Italy (Lago Grande di Monticchio) during the periods 100–75 ka BP and 14 ka BP to present, while steppes dominated shortly around 95 ka BP and between 75 and 14 ka (Figure 13; Allen *et al.*, 1999). No detailed investigation of the vegetation history is available for the Sila upland over the last 100 ka and so far, only palaeopedological investigations are available (Scarciglia *et al.*, 2005b, 2008). Detailed soil charcoal analyses at Cecita Lake has enabled the reconstruction of vegetation changes for

© 2019 John Wiley & Sons, Ltd.

Earth Surf. Process. Landforms, Vol. **44**, 2570–2586 (2019)
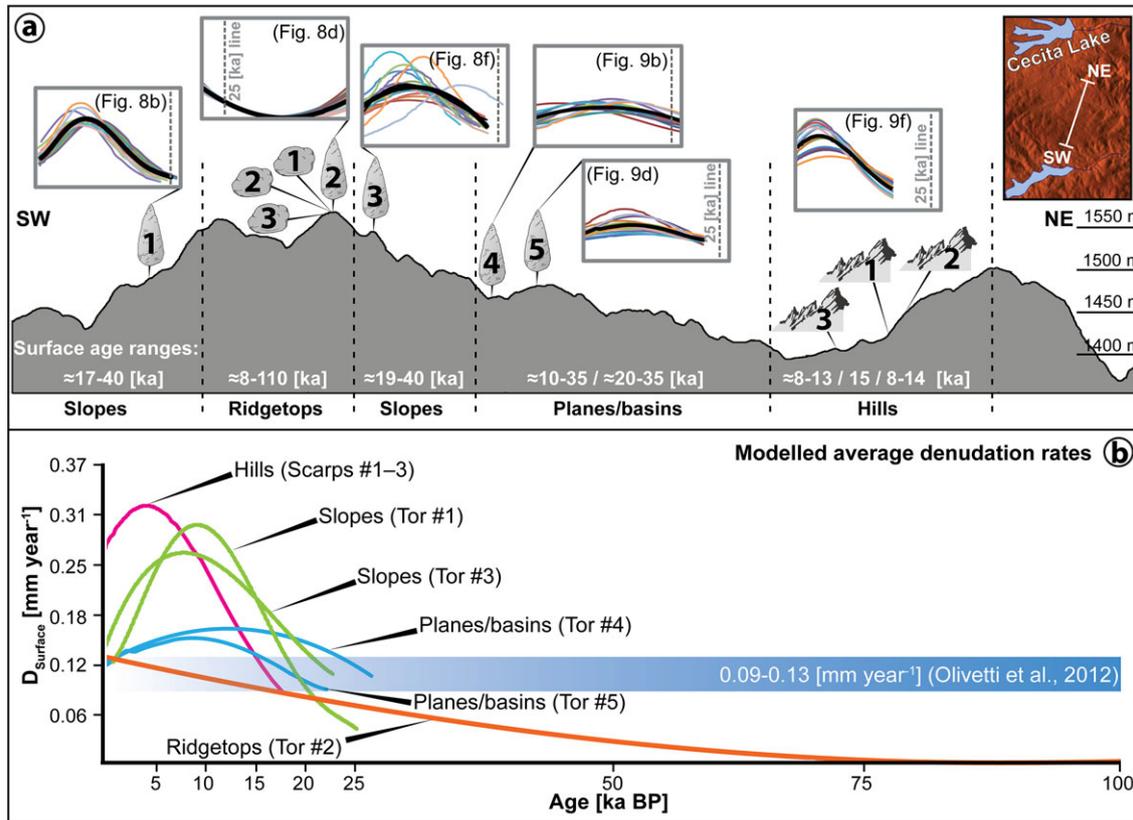
Figure 12. (a) Relation between surface topography and denudation rates along the southwest–northeast (SW–NE) investigation transect. (b) Comparison of modelled average denudation rates over time (Figures 8 and 9) of the different surface relief sections (e.g. ridgetops, slopes, planes/basins, hills) and average erosion rates (calculated from cosmogenic ^{10}Be concentration using a material density of 2.6 g cm^{-3}) after Olivetti *et al.* (2012). [Colour figure can be viewed at wileyonlinelibrary.com]
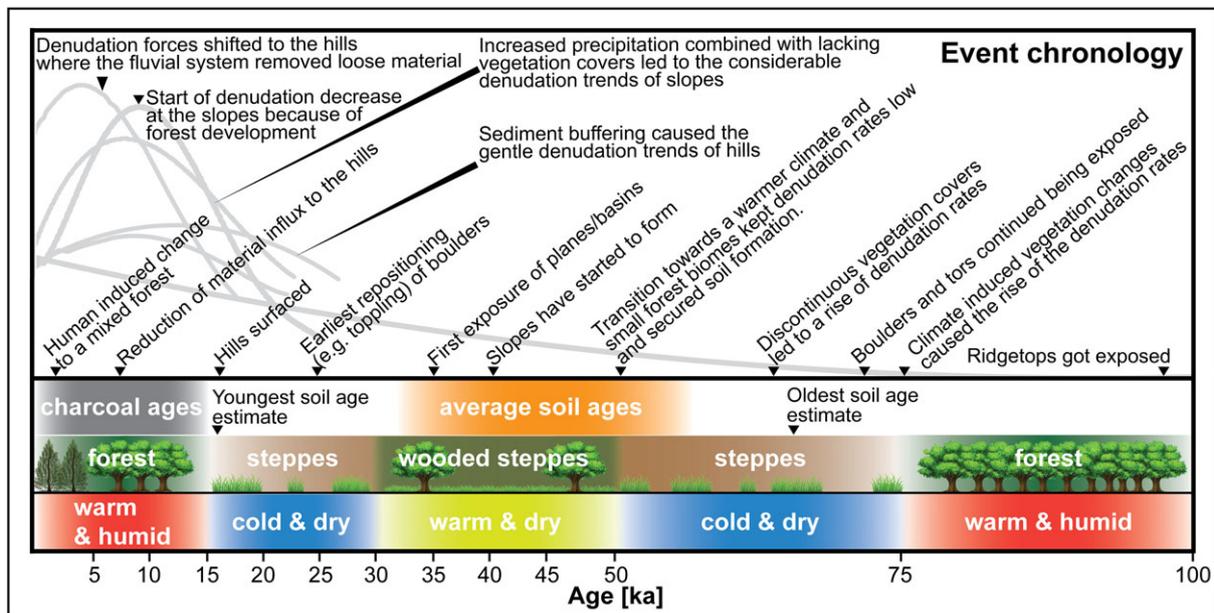
Figure 13. Model of local changes in climate (Allen *et al.*, 1999) and vegetation (Allen *et al.*, 1999; Pelle *et al.*, 2013) for the last 100 ka. This concept also includes soil and charcoal ages and major findings of Raab *et al.* (2017) and Moser *et al.* (2017) to complement the series of surface evolution events. [Colour figure can be viewed at wileyonlinelibrary.com]

the Holocene (Moser *et al.*, 2017). Fragments of charcoal in the soils surrounding Cecita Lake indicated the presence of an oak-dominated deciduous forest, which since has been replaced by mountain pine forest (Figure 13; Pelle *et al.*, 2013). Calibrated carbon-14 (^{14}C) ages of charcoal samples only gave ages no older than 14 ka (Moser *et al.*, 2017), which correlate with our surface exposure ages of the hills (8–15 ka; Figure 12a).

These data are consistent with those obtained from pollen analyses of a nearby upland palaeolake (Trifoglietti) of the Coastal Chain, located about 50 km northwest of our study area. Joannin *et al.* (2012) found evidence of an increased moisture from about 11 to 9.4 ka cal BP which could have enhanced erosion processes. At this site, a period with maximum humidity is recorded around 9.4–6.2 ka cal BP, followed by a general trend

towards a drier climate until present. Previous soil age-estimates in the range 16–67 ka BP with an average of 45 ± 11 ka BP (Figure 13; Raab *et al.*, 2017) in the Sila upland correspond to the age of the slopes (~40 ka; Figure 12a). Additionally, a relatively short warmer and drier climate pulse from 30 to 50 ka BP enabled wooded steppes to form here (Figure 13; Allen *et al.*, 1999) which would have slightly balanced the denuding processes through a denser root network that would have withheld soil and sediment. Furthermore, soil development is strongly linked with volcanic ash influx during this time (Raab *et al.*, 2018). Fertilization through volcanic ash-inputs (Pelle *et al.*, 2013; Raab *et al.*, 2017, 2018) may have enhanced this development at the upland, and might help explain the low $D_{Surface}$ of Tor #2 (Figures 5d and 12b).

Studies of human activity in southern Italy indicate the presence of organized human societies since 6–7 ka BP (Scarciglia *et al.*, 2008; Pelle *et al.*, 2013; Russo Ermolli *et al.*, 2018). Allen *et al.* (1999) and Russo Ermolli *et al.* (2018) showed that the Apennine mountain chain and the Sant'Eufemia Plain (located southwest of the Sila Massif) experienced an increased influence of agricultural and forest clearance for the last 2 ka. A drastic increase in soil erosion has been recorded by Raab *et al.* (2018) due to more recent human activities.

Conclusions

Surface exposure dating (^{10}Be) along vertical rock profiles of granitic landscape forms (tors, boulders, scarps) revealed the temporal sequence of soil denudation processes and thus the controls on landscape evolution of the Sila Massif in southern Italy.

Tors provide a detailed insight into landscape evolution for the last 100 ka in southern Italy and allow us to more clearly understand and more effectively quantify the impacts that environmental factors have on landscape evolution here. We consider these granitic features to be a very useful *in situ* landscape archive that provide evidence of variable rates of soil denudation over time and as a function of topographic position. We see, furthermore, a great potential in this approach to trace and quantify over long periods of time the influence of climate variability on landscape denudation rates. This in turn is crucial for predicting the effect of future climate change on soil erosion rates. Our modelled soil denudation rates vary across a range of *c.* 0 to 0.37 mm yr^{-1}, with the highest rates occurring around 10–25 ka BP.

Boulders, however, may not remain at a stable position and are therefore less suitable for dating these landscape processes. The investigated boulders in the Sila upland evolved parallel to the tors, although some appear to have experienced changes in position about 20–25 ka BP, making the calculation of soil denudation rates difficult or impossible at this point in time. The investigated rock scarps in the Sila upland are relatively young (8–15 ka) and show a rather abrupt bedrock exposure, probably due to an increase of the denudation forces during the last 15 ka, with a maximum at ~5 ka BP. Thus, the scarps at the Sila upland represent the final stage of surface evolution, probably triggered by an initial river incision, while boulder and tors are remnants of an older landscape where surface lowering (denudation) prevailed.

By piecing together the evolution of the individual landforms, we are able to reconstruct a denudation chronology for the Sila upland for the last 100 ka and to relate it to environmental processes that appear to drive the evolution of this landscape. Climate induced vegetation changes around 75 ka BP

and rapid changes towards warmer and more humid conditions around 15 ka BP appear responsible for the increases in denudation rates where we observed them. Increases in the density of vegetation cover (e.g. forest) from 30 to 50 ka BP and particularly after 15 ka BP appears to have counteracted erosion during these periods. Topography was apparently a secondary factor controlling the extent of past variability in denudation rates in the upland. Our data suggest that slopes previously have experienced higher denudation rates than present-day planes and basins.

Overall, tors, boulder and scarps of granitic landscapes are excellent archives with which we may reconstruct environmental processes over time that may greatly improve our understanding of surface mass-flux processes.

References

Allen JRM, Brandt U, Brauer A, Hubberten HW, Hunley B, Keller J, Kraml M, Mackensen A, Mingram J, Negendank JFW, Nowaczyk NR, Oberhänsli H, Watts WA, Wulf S, Zolitschka B. 1999. Rapid environment changes in southern Europe during the last glacial period. *Nature* **400**: 740–743. https://doi.org/10.1038/23432.

Bajard M, Poulenard J, Sabatier P, Develle AL, Giguet-Covex C, Jacob J, Crouzet C, David F, Pignol C, Arnaud F. 2017. Progressive and regressive soil evolution phases in the Anthropocene. *Catena* **150**: 39–52. https://doi.org/10.1016/j.catena.2016.11.001.

Balco G, Stone JO, Lifton NA, Dunai TJ. 2008. A complete and easily accessible means of calculating surface exposure ages or erosion rates from ^{10}Be and ^{26}Al measurements. *Quaternary Geochronology* **8**: 174–195. https://doi.org/10.1016/j.quageo.2007.12.001.

Bates RL, Jackson JA. 1987. *Glossary of Geolgoy*, third edn. Alexandria, VA: American Geological Institute.

Bintanja R, Roderik SW, Oerlemans J. 2005. Modelled atmospheric temperatures and global sea levels over the million years. *Nature* **437**: 125–128. https://doi.org/10.1038/nature03975.

Bonin G. 1981. L'étagement de la végétation dans l'Apennin méridional. *Ecologia Mediterranea* **7**: 79–91.

Borchers B, Marrero S, Balco G, Caffee M, Goehring B, Lifton N, Nishiizumi K, Phillips F, Schaefer J, Stone J. 2016. Geological calibration of spallation production rates in the CRONUS-Earth. *Quaternary Geochronology* **31**: 188–198. https://doi.org/10.1016/j.quageo.2015.01.009.

Brown ET, Edmond JM, Raisbeck GM, Yiou F, Desgarceaux S. 1992. Effective attenuation length of cosmic rays producing ^{10}Be and ^{26}Al in quartz: implications for surface exposure dating. *Geophysical Research Letters* **9**: 369–372. https://doi.org/10.1029/92GL00266.

Chmeleff J, von Blanckenburg F, Kossert K, Jakob D. 2010. Determination of the ^{10}Be half-life by multicollector ICP-MS and liquid scintillation counting. *Nuclear Instruments and Methods in Physics Research Section B: Bean Interaction with Materials and Atoms* **268**: 192–199. https://doi.org/10.1016/j.nimb.2009.09.012.

Christl M, Vockenhuber C, Kubik PQ, Wacker L, Lachner J, Alfimov V, Synal HA. 2013. The ETH Zurich AMS facilities: performance parameters and reference materials. *Nuclear Instruments and Methods in Physics Research B* **294**: 29–38. https://doi.org/10.1016/j.nimb.2012.03.004.

Combourieu-Nebout N. 1993. Vegetation response to upper Pliocene glacial/interglacial cyclicity in the central Mediterranean. *Quaternary Research* **40**: 228–236. https://doi.org/10.1006/qres.1993.1074.

Corbi F, Fubelli G, Lucá F, Muto F, Pelle T, Robustelli G, Scarciglia F, Drams F. 2009. Vertical movements in the Ionian margin of the Sila

Massif (Calabria, Italy). *Bollettino della Socieà Geologica Italina* **128**: 731–738. https://doi.org/10.3301/IJG.2009.128.3.731.

Fauquette S, Combourieu-Nebout N. 2013. Palaeoaltitude of the Sila Massif (Southern Apennines, Italy) and distribution of the vegetation belts at ca. 2.4 Ma (Early Pleistocene). *Review of Palaeobotany and Palynology* **189**: 1–7. https://doi.org/10.1016/j.revpalbo.2012.10.003.

Gosse JC, Philips FM. 2001. Terrestrial in situ produced cosmogenic nuclids: theory and application. *Quaternary Science Reviews* **20**: 1475–1560. https://doi.org/10.1016/S0277-3791(00)00171-2.

Gunnell Y, Jarman D, Braucher R, Calvet M, Delmas M, Leanni L, Bourlès D, Arnold M, Aumaitre G, Keddaouche K. 2013. The granite tors of Dartmoor, Southwest England: rapid and recent emergence revealed by Late Pleistocene cosmogenic apparent exposure ages. *Quaternary Science Reviews* **61**: 62–76. https://doi.org/10.1016/j.auascirev.2012.11.005.

Heimsath AM, Chappell J, Dietrich WE, Nishiizumi K, Finkel RC. 2001. Late Quaternary erosion in southeastern Australia: a field example using cosmogenic nuclides. *Quaternary International* **83**: 169–185. https://doi.org/10.1016/S1040-6182(01)00038-6.

Joannin S, Brugiapaglia E, De Bealieu JL, Bernardo L, Magny M, Peyron O, Goring S, Vannière B. 2012. Pollen-based reconstruction of Holocene vegetation and climate in southern Italy: the case of Lago Trifoglietti. *Climate of the Past* **8**: 1973–1996.

Kitchener JA. 1984. The froth flotation process: past, present and future – in brief. In *The Scientific Basis of Flotation*, Ives KJ (ed.), NATO ASI Series (Series E: Applied Sciences) 75. Springer: Dordrecht. https://doi.org/10.1007/978-94-009-6926-1_2

Kohl C, Nishiizumi K. 1992. Chemical isolation of quartz for measurement of in-situ –produced cosmogenic nuclides. *Geochimica Cosmochimica Acta* **56**: 3583–3587. https://doi.org/10.1016/0016-7037(92)90401-4.

Korschinek G, Bergmaier A, Faestermann T, Gerstmann UC, Remmert A. 2010. A new value for the half-life of ^{10}Be by heavy-ion elastic recoil detection and liquid scintillation counting. *Nuclear Instruments and Methods in Physics Research Section B: Bean Interaction with Materials and Atoms* **268**: 187–191. https://doi.org/10.1016/j.nimb.2009.09.020.

Kubik PW, Christl M. 2010. ^{10}Be and ^{26}Al measurements at the Zurich 6 MV Tandem AMS facility. *Nuclear Instruments and Methods B* **268**: 880–883. https://doi.org/10.1016/j.nimb.2009.10.054.

Le Pera E, Sorriso-Valvo M. 2000. Weathering and morphogenesis in a Mediterranean climate, Calabria, Italy. *Geomorphology* **34**(3): 251–270. https://doi.org/10.1016/S0169-555X(00)00012-X.

Lichter J. 1998. Rates of weathering and chemical depletion in soils across a chronosequence of Lake Michigan sand dunes. *Geoderma* **85**: 255–282. https://doi.org/10.1016/S0016-7061(98)00026-3.

Linton DL. 1955. The problem of tors. *The Geographical Journal* **121**: 470–481.

Liotta D, Caggianelli A, Kruhl JH, Festa V, Prosser G, Langoe A. 2008. Multiple injections of magmas along a Hercynian mid-crustal shear zone (Sila Massif, Calabria, Italy). *Journal of Structural Geology* **30**: 1202–1217. https://doi.org/10.1016/j.jsg.2008.04.005.

Masarik J, Frank M, Schaefer JM, Wieler R. 2001. Correction of in-situ cosmogenic nuclide production rates for geomagnetic field intensity variations during the past 800,000 years. *Geochimica et Cosmochimica Acta* **65**: 2995–3003.

Middlemost EAK. 1994. Naming materials in the magma/igneous rock system. *Earth-Science Reviews* **37**: 215–224.

Migoń P. 2006. *Granite Landscapes of the World*. Oxford University Press: New York.

Migoń P. 2013. Weathering and hillslope development. In *Treatise on Geomorphology*, Shroder JF (ed.). Academic Press: San Diego, CA; volume **4**, 159–178. https://doi.org/10.1016/B978-0-12-374739-6.00075-0

Migoń P, Prokop P. 2013. Landforms and landscape evolution in the Mylliem Granite Area, Meghalaya Plateau, northeast India. *Singapore Journal of Tropical Geography* **34**: 206–228.

Migoń P, Vieira G. 2014. Granite geomorphology and its geological controls, Serra da Estrela, Portugal. *Geomorphology* **226**: 1–14. https://doi.org/10.1016/j.geomorph.2014.07.027.

Molin P, Pazzaglia FJ, Dramis F. 2004. Geomorphic expression of active tectonics in a rapidly-deforming fore-arc, Sila Massif, Calabria,

southern Italy. *American Journal of Science* **304**: 559–589. https://doi.org/10.2475/ajs.304.7.559.

Moser D, Di Pasquale G, Scarciglia F, Nelle O. 2017. Holocene mountain forest changes in central Mediterranean: soil charcoal data from the Sila Massif (Calabria, southern Italy). *Quaternary International* **457**: 113–130. https://doi.org/10.1016/j.quaint.2017.01.042.

Nishiizumi K, Imamura M, Caffee MW, Southon JR, Finkel RC, McAnich J. 2007. Absolut calibration of ^{10}Be AMS standards. *Nuclear Instruments & Methods in Physics Research Section B-Beam Interactions with Materials and Atoms* **258**: 403–413. https://doi.org/10.1016/j.nimb.2007.01.297.

Olivetti V, Cyr AJ, Molin P, Faccenna C, Granger DE. 2012. Uplift history of the Sila Massif, southern Italy, deciphered from cosmogenic ^{10}Be erosion rates and river longitudinal profile analysis. *Tectonics* **31**: 1–19. https://doi.org/10.1029/2011TC003037.

Ozenda P. 1975. Sur les étages de vegetation dans le montagnes du basin méditerranéen. *Documents Cartographiques Ecologiques (Grenoble)* **16**: 1–32.

Pelle T, Scarciglia F, Di Pasquale G, Allevato E, Marino D, Robustelli G, La Russa MF, Pulice I. 2013. Multidisciplinary study of Holocene archaeological soils in an upland Mediterranean site: natural versus anthropogenic environmental changes at Cecita Lake, Calabria, Italy. *Quaternary International* **303**: 163–179. https://doi.org/10.1016/j.quaint.2013.04.003Sc.

Perri F, Critelli S, Dominici R, Muto F, Tripodi V, Ceramicola S. 2012. Provenance and accommodation pathways of late Quaternary sediments in the deep-water northern Ionian Basin, southern Italy. *Sedimentary Geology* **280**: 244–259.

Phillips WM, Hall AM, Mottram R, Fifield LK, Sugden DE. 2006. Cosmogenic ^{10}Be and ^{26}Al exposure ages of tors and erratics, Cairngorm Mountains, Scotland: timescales for the development of a classic landscape of selective linear glacial erosion. *Geomorphology* **73**: 222–245. https://doi.org/10.1016/j.geomorph.2005.06.009.

Pigati JS, Lifton NA. 2004. Geomagnetic effects on time-integrated cosmogenic nuclide production with emphasis on in situ ^{14}C and ^{10}B. *Earth and Planetary Science Letters* **226**: 193–205. https://doi.org/10.1016/j.epsl.2004.07.031.

Raab G, Halpern D, Scarciglia F, Raimondi S, Norton K, Pettke T, Hermann J, de Castro PR, Aguilar Sanchez AM, Egli M. 2017. Linking tephrochronology and soil characteristics in the Sila and Nebrodi mountains, Italy. *Catena* **158**: 266–285. https://doi.org/10.1016/j.catena.2017.07.008.

Raab G, Scarciglia F, Norton K, Dahms D, Brandová D, de Castro PR, Christl M, Ketterer ME, Ruppli A, Egli M. 2018. Denudation variability of the Sila Massif upland (Italy) from decades to millennia using ^{10}Be and $^{239+240}$Pu. *Land Degradation and Development* **29**(10): 3736–3752. https://doi.org/10.1002/ldr.3120.

Ruello MR, Cinque A, Di Donato V, Molisso F, Terrasi F, Russo Ermolli E. 2017. Interplay between sea level rise and tectonics in the Holocene evolution of the St. Eufemia Plain (Calabria, Italy). *Journal of Coastal Conservation* **21**: 903–915. https://doi.org/10.1007/s11852-017-0558-9.

Russo Ermolli E, Ruello MR, Cicala L, Di Lorenzo H, Moilsso F, Pacciarelli M. 2018. An 8300-yr record of environmental and cultural changes in the Sant'Eufemia Plain (Calabria, Italy). *Quaternary International* **483**: 39–56.

Scarciglia F. 2015. Weathering and exhumation history of the Sila Massif upland plateaus, southern Italy: a geomorphological and pedological perspective. *Journal of Soils and Sediments* **15**: 1278–1291. https://doi.org/10.1007/s11368-014-0923-3.

Scarciglia F, Le Pera E, Critelli S. 2005a. Weathering and pedogenesis in the Sila Grande Massif (Calabria, south Italy): from field scale to micromorphology. *Catena* **61**: 1–29. https://doi.org/10.1016/j.catena.2005.02.001.

Scarciglia F, Le Pera E, Vecchio G, Critelli S. 2005b. The interplay of geomorphic processes and soil development in an upland environment, Calabria, south Italy. *Geomorphology* **69**: 169–190. https://doi.org/10.1016/j.geomorph.2005.01.003.

Scarciglia F, Le Pera E, Critelli S. 2007. The onset of the sedimentary cycle in a mid-latitude upland environment: weathering, pedogenesis and geomorphic processes on plutonic rocks (Sila Massif, Calabria). In *Sedimentary Provenance and Petrogenesis: Perspectives from Petrography and Geochemistry*, Arribas J, Critelli S, Johnsson MJ

© 2019 John Wiley & Sons, Ltd.

Earth Surf. Process. Landforms, Vol. **44**, 2570–2586 (2019)

(eds), Geological Society of America Special Paper 420. Geological Society of America: Boulder, CO; 149–166. https://doi.org/10.1130/2006.2420(10)

Scarciglia F, De Rosa R, Vecchio G, Apollaro C, Robustelli G, Terrasi F. 2008. Volcanic soil formation in Calabria (southern Italy): the Cecita Lake geosol in the late Quaternary geomorphological evolution of the Sila uplands. *Journal of Volcanology Geothermal Research* **177**: 101–117. https://doi.org/10.1016/j.jvolgeores.2007.10.014.

Scarciglia F, Critelli S, Borrelli L, Coniglio S, Muto F, Perri F. 2016. Weathering profiles in granitoid rocks of the Sila Massif uplands, Calabria, southern Italy: new insights into their formation process and rates. *Sedimentary Geology* **336**: 46–67. https://doi.org/10.1016/j.sedgeo.2016.01.015.

Small EE, Anderson RS, Hancock GS. 1999. Estimates of the rate of regolith production using ^{10}Be and ^{26}Al from an alpine hillslope. *Geomorphology* **27**: 131–150. https://doi.org/10.1016/So169-55x(98)00094-4.

Smithson P, Addison K, Atkinson K. 2013. *Fundamentals of the Physical Environment – Fourth Edition.* London: Routledge.

Sorriso-Valvo M. 1993. The geomorphology of Calabria. A sketch. *Geografia Fisica e Dinamica Quaternaria* **16**: 75–80.

Spina V, Galli P, Tondi M, Critelli S, Cello G. 2007. Kinematics and structural properties of an active fault zone in the Sila Massif (northern Calabria, Italy). *Bollettino della Società Geologica Italiana* **126**: 427–438.

Stone JO. 2000. Air pressure and cosmogenic isotope production. *Journal of Geophysical Research* **105**: 753–759. https://doi.org/10.1029/2000JB900181.

Thomas MF. 1965. Some aspects of the geomorphology of domes and tors in Nigeria. *Zeitschrift für Geomorphologie N.F* **9**: 63–81.

Thomas MF. 1997. Weathering and landslides in the humid tropics: a geomorphological perspective. *Journal of the Geosocial Society of China* **40**: 1–16.

Twidale CR. 2002. The two-stage concept of landform and landscape development involving etching: origin, development and implications of an idea. *Earth Science Reviews* **57**: 37–74. https://doi.org/10.1016/S0012-8252(01)00059-9.

Twidale CR, Romaní JRV. 2005. *Landforms and Geology of Granite Terrains.* Taylor & Francis: London.

von Blanckenburg F, Belshaw NS, O'Nions RK. 1996. Separation of 9Be and cosmogenic 10Be from environmental materials and SIMS isotope dilution analysis. *Chemical Geology* **129**: 93–99. https://doi.org/10.1016/0009-2541(95)00157-3.

von Eynatten H, Tolosana-Delgado R, Karius V, Bachmann K, Caracciolo K. 2015. Sediment generation in humid Mediterranean setting: grain-size and source-rock control on sediment geochemistry and mineralogy (Sila Massif, Calabria). *Sedimentary Geology* **336**: 68–80. https://doi.org/10.1016/j.sedgeo.2015.10.008.

Wakasa S, Matsuzaki H, Tanaka Y, Matsukura Y. 2006. Estimation of episodic exfoliation rates of rock sheets on a granite dome in Korea from cosmogenic nuclide analysis. *Earth Surface Processes and Landforms* **31**: 1246–1256. https://doi.org/10.1002/esp.1328.

Supporting Information

Additional supporting information may be found online in the Supporting Information section at the end of the article.

TABLE S1. Input data for the CRONUS online calculator (Balco et al., 2008).

© 2019 John Wiley & Sons, Ltd.

Earth Surf. Process. Landforms, Vol. **44**, 2570–2586 (2019)